INFLUENCE OF HORIZONTAL MODEL RESOLUTION ON THE SPATIAL SCALE OF EXTREME PRECIPITATION EVENTS

Syed Muhammad Anas Ali

A THESIS SUBMITTED TO

THE FACULTY OF GRADUATE STUDIES

IN PARTIAL FULFILMENT OF THE REQUIREMENTS

FOR THE DEGREE OF

MASTER OF SCIENCE

GRADUATE PROGRAM IN EARTH AND SPACE SCIENCE

YORK UNIVERSITY

TORONTO, ONTARIO

June 2023

Abstract

Previous work has shown that strong ascending motion is a key driver of extreme precipitation events (EPEs). Thus, the horizontal spatial scales of this "extreme ascent" are likely important for determining the spatial scales of EPEs. Therefore, understanding how climate models capture horizontal scales of ascending anomalies is critical to understanding and assessing climate models' simulations and projections of extreme precipitation. Analyzing daily output from 27 models participating in the Coupled Model Intercomparison Project phase 6 (CMIP6) and High-Resolution Model Intercomparison Project (HighResMIP), we show that horizontal model resolution is a key influence on the horizontal scales of extreme ascent. We compute the horizontal scale for a given EPE as the e-folding distance of the vertical velocity anomaly on the day of the EPE, which is scaled to produce an inverse wavenumber. We then composite these horizontal scales over all annual maximum EPEs between 1981 and 2000 for each model. We focused on the horizontal scale zonally averaged over the 40°S-55°S latitude band. Our analysis suggests that model horizontal resolution places an upper limit on the horizontal scale of extreme ascent. Models with

around 150 longitude points (approximately 153 km resolution at 55°S) have mean horizontal scales topping out at approximately 320 km, and this upper limit decreases to approximately 220 km for models with 500 longitude points (approximately 46 km resolution at 55°S). Additional analysis shows that the horizontal scales for geopotential anomalies during EPEs have no clear resolution dependence. However, the horizontal scales of geopotential were generally larger (700-1100 km) than those for vertical velocity or precipitation anomalies, and more in line with theoretical expectations based on the Rossby radius of deformation. Additional insight is gained through analysis of grid-scale and convective precipitation. Altogether, these results suggest that the simulated large-scale dynamics associated with EPEs is realistic, but the models are convecting at the grid scale rather than sub-grid scale. This is unrealistic as convective precipitation is expected to contribute strongly to extreme precipitation events. Additional analysis ensured that our results were not just a product of grid box storms, and that they were not sensitive to internal variability or temporal resolution.

Dedication

For my family, friends, peers, and mentors.

Acknowledgements

I want to acknowledge my parents who have supported me throughout my academic career and continue to do so. I also want to acknowledge Professor Tandon, who was the most important person to the success and completion of this thesis. I also want to thank and acknowledge Professor Klaassen, who served on my supervisory committee and provided many new questions and insights. I would also like to acknowledge my colleagues in Professor Tandon's group, Noah and Thabo, whose support and experience was invaluable to me.

Contents

List of Tables

List of Figures

1 Introduction

1.1 Brief Overview

Extreme precipitation is of great human interest because of the potentially severe consequences extreme precipitation events can have. For example, extreme precipitation caused the Pakistan floods of 2010, which lead to 1700 deaths and the damage or complete destruction of one million homes (Kirsch et al., 2012). The Alberta floods of 2013 were also caused by extreme precipitation and were the costliest disaster in Canadian history up until that time (Milrad, Gyakum, & Atallah, 2015). Thus, it is crucial to understand, project and prepare for extreme precipitation events to limit their consequences. While extreme precipitation events are projected to intensify over most regions under climate change based on thermodynamic principles, these projections are regionally dependent. Previous work in the field has shown that this regional variability is influenced by changes in the ascent associated with extreme precipitation events (referred to as "extreme ascent"). Moreover, earlier research has suggested that changes in extreme ascent are influenced by changes in the horizontal scale of ascent, which corresponds to the spatial size of a storm. Furthermore, the spatial scale of a storm closely relates to the timescale of a storm, which in turn influences the accumulated precipitation during the storm. Thus, understanding the horizontal scale of extreme ascent is critical to understanding and projecting extreme precipitation. Climate models are the primary tools for studying the spatial scales for extreme ascent. However, as with any application of models, it is important to first determine how models differ and to what extent they can be trusted. To this end, this thesis asks: what is the influence of horizontal model resolution on the spatial scales of extreme ascent and other quantities associated with extreme precipitation events?

Firstly, this introductory chapter gives an overview of various theoretical topics relevant to this thesis. Then, the Chapter 2 explains the datasets used in this study and the process through which horizontal scales are computed from model output. Chapter 3 presents the findings of the analysis, beginning with the horizontal scales of ascent. The results will show a clear model resolution influence on the horizontal scales of ascent and precipitation, and that the models are unrealistically convecting at the grid scale rather than the sub grid scale. Finally, Chapter 4 summarizes the findings of this thesis and considers some limitation and potential extensions of the analysis.

The remainder of this introduction provides a theoretical overview of several relevant background topics. Section 1.2 begins to introduce extreme precipitation by covering the Clausius-Clapeyron equation, which relates rising temperatures under climate change to a projection of increasing extreme precipitation intensity through thermodynamical effects. Section 1.3 introduces the basics of the hydrological cycle and section 1.4 covers the general global structure of precipitation. While the previous two sections focus on annual means, section 1.5 considers annual variation in local hydrology. Section 1.6 then covers the basics of the global atmospheric circulation, focusing on large scale phenomena like the Hadley cells, Ferrel cells, and eddies. Then, section 1.7 explains how ascent contributes dynamical effects to precipitation which lead to regional variability in the projections. Section 1.8 then introduces the quasigeostrophic omega equation, a theoretical tool for studying the mechanisms that drive vertical velocity at the synoptic scale. Section 1.9 then uses the quasi-geostrophic omega equation to relate extreme ascent to the horizontal scale of ascent and explains some of the drivers of changes in the horizontal scale of ascent. While this thesis focuses on spatial scales, section 1.10 briefly considers temporal scales of extreme precipitation events. Section 1.11 then gives a brief overview of intensity-duration-frequency (IDF) curves, graphical tools that show the relative rarity of observed precipitation events by considering their intensity, duration, and frequency. Finally, to connect the theoretical discussion to modelling, I give a brief introduction to models' representation of the atmosphere in section 1.12.

1.2 The Clausius-Clapeyron Relationship

Under climate change, extreme precipitation events are projected to intensify (Kharin et al., 2013). This expectation follows from the thermodynamic Clausius-Clapeyron relationship, which relates temperature to saturation vapour pressure. Vapour pressure is the pressure that the water vapour in an air parcel would exert if alone in the volume, while saturation vapour pressure is the pressure exerted when an air parcel is fully saturated. A saturated parcel is one where the vapour and liquid phases are in equilibrium (as many molecules are returning to the liquid as there are escaping as vapour).

Equation 1.1 shows the general form of the Clausius-Clapeyron equation, where e_s is the saturation vapor pressure, T is temperature, l_v is the latent heat of vaporization, T is temperature, and R_v is the ideal gas constant for water vapour. For terrestrial conditions, and assuming that l_v is approximately constant with temperature, the equation can be solved to a good approximation given by equation 1.2, where e_{s0} is a constant.

$$\frac{de_s}{dT} = \frac{l_v e_s}{R_v T^2} \tag{1.1}$$

$$e_s \approx e_{s0} \times \exp\left(\frac{l_v}{R_v}\left[\frac{1}{273} - \frac{1}{T}\right]\right) \tag{1.2}$$

The Clausius-Clapeyron relationship shows that saturation vapour pressure increases approximately exponentially with changes in temperature, meaning that warmer air parcels can take on exponentially more moisture than cooler air parcels. Thus, extreme precipitation events are projected to intensify under climate change following first principles (assuming that relative humidity stays constant): as the atmosphere warms, the saturation vapour pressure of the atmosphere increases, leading to more moisture available in the atmosphere for condensation, ultimately allowing for more intense extreme precipitation events. This thermodynamic Clausius-Clapeyron effect leads to a well understood global scaling of precipitation intensity under climate change (Pfahl, O'Gorman, & Fischer, 2017). However, as explained in section 1.7, this scaling does not capture all the mechanisms driving extreme precipitation changes.

1.3 The Hydrologic Cycle

The hydrologic cycle, also known as the water cycle, is the continuous cycling of water on Earth between bodies of water, the ground, and the atmosphere. As the total water on Earth is conserved, the hydrologic cycle captures the exchange of water between these reservoirs. The main general features of the hydrologic cycle are evaporation and vertical transport which bring moisture at or near the surface higher into the atmosphere, precipitation which brings moisture from the atmosphere back to the surface, run off which transports moisture through the land, and horizontal transport through the atmosphere. For local climates, equation 1.3 (Hartmann, 2016) describes the relevant water balance for the surface, where g_w is stored groundwater, P is precipitation, D is the surface condensation from dewfall or frost, E is evapotranspiration, and Δf is runoff.

$$g_w = P + D - E - \Delta f \tag{1.3}$$

While evaporation captures the transformation of liquid surface water to water vapour, evapotranspiration includes water surface evaporation, soil moisture evaporation, and plant transpiration (the release of water vapour by plants). Over long term averages the storage term is small and dewfall can be incorporated into the precipitation or neglected, simplifying equation 1.3 to equation 1.4 (Hartmann, 2016), which introduces the famous $P - E$ quantity.

$$\Delta f = P - E \tag{1.4}$$

Figure 1.1 is taken from Hartmann (2016) and shows the zonal means of the components of equation 1.4. The $P - E$ quantity in figure 1.1 follows much of the intuition one has about wet and dry climates, with positive $P - E$ around the equator and in the middle to high latitudes, and negative $P-E$ between the 15° to 40° latitude band in each hemisphere. The peak in P around the equator is mostly associated with the intertropical convergence zone (ITCZ).

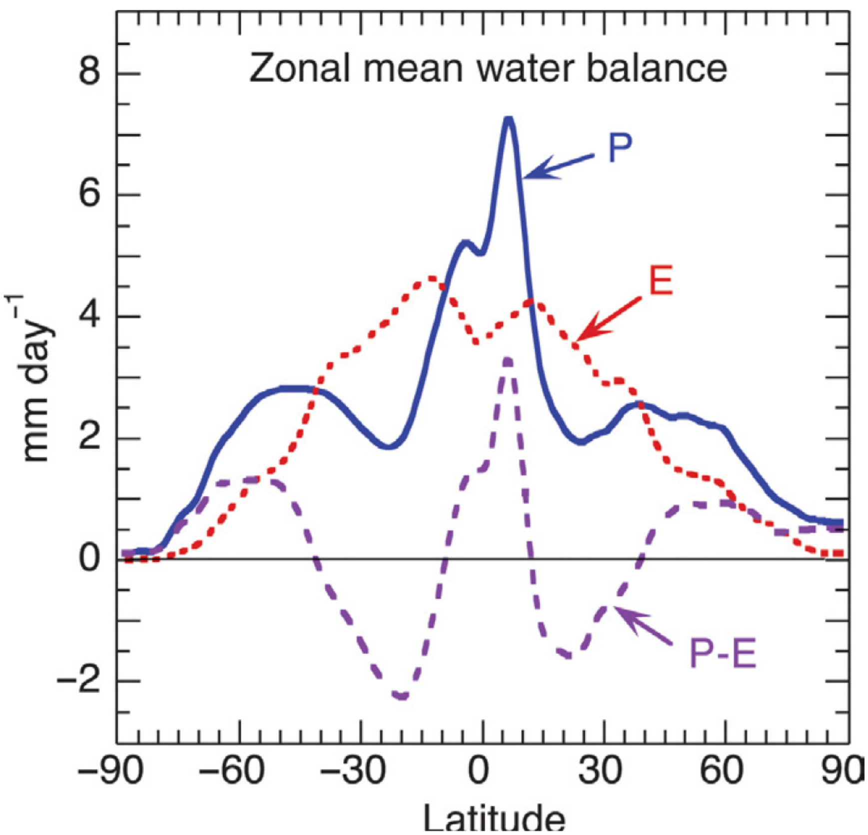

Figure 1.1: Figure 5.2 from Hartmann (2016), showing zonal means of evaporation E, precipitation P, and $P - E$ using data from ERA Interim 1979-2009.

1.4 Global Precipitation

The mechanism through which moisture in the atmosphere becomes precipitation is generally simple: moist air parcels become supersaturated, allowing water vapour to condense into droplets that fall when they are large and heavy enough to overcome the ascent (or updrafts in a cloud) that the air parcels experience. Supersaturation occurs when the specific humidity of a parcel (the ratio of the mass of water vapour to the mass of air) exceeds that at saturation. Supersaturation in the atmosphere is usually reached through adiabatic cooling as the air parcels expand and become less dense during ascent. How the moisture gets into the middle and upper troposphere is less simple as there are various potential mechanisms that have varying significance depending on location or season. For example, in the midlatitudes, atmospheric motion associated with both frontal and synoptic weather systems can force parcels to ascend (Hartmann, 2016). In the tropics and over continents, convective instability generates buoyancy in cumulonimbus clouds and forces parcels upward, driving much of the precipitation (Hartmann, 2016).

Figure 1.2 shows annual mean precipitation. This shows many of the same features as in figure 1.1, such as the precipitation peak near the equator. High temperatures near the equator lead to air with high water content (following the Clausius-Clapyeron relation), and tropical convective systems produce the ascent that drives much of the precipitation systems around the equator. In contrast, precipitation is weak towards the poles, where less solar heat leads to lower temperatures and thus a lower water content for the air. In the tropics, precipitation is highest around the Maritime Continent and over the land in South America and Africa, in part due to the Walker circulation. The Walker circulation is a large scale circulation that is driven by upwelling and downwelling in the ocean. Warm surface water collects near the Maritime Continent and cooler surface water collects near South America, the temperature difference associated with this upwelling and downwelling in turn creates a pressure gradient in the atmosphere, with high pressure over the Maritime Continent and low pressure over South America. Closer to the surface, this pressure gradient is reversed with low pressure over the Maritime continent and high pressure over South America. Thus, the rising branch of the Walker circulation is over the Maritime continent where warm humid air rises higher into the atmosphere (from low to high pressure), driving high precipitation. The air higher in the atmosphere then moves towards South America (from high to low pressure) before descending (from low to high pressure). The high precipitation in parts of the eastern halves of the Pacific and Atlantic oceans is associated with the ITCZ, though some regions near the equator in the eastern Pacific and Atlantic oceans are very dry. This high tropical precipitation moves north and south to follow solar heating from the sun. While the ITCZ is generally slightly north of the equator, the South Pacific Convergence Zone (SPCZ) is slightly south of the equator and spans towards the mid-latitudes. The mid-latitudes of the Northern Hemisphere show the highest precipitation along the western coast where storm tracks form. In contrast, the mid-latitudes of the Southern Hemisphere show high precipitation across all longitudes. Mid-latitude weather systems can force ascent, and when combined with westerly flow over mountain ranges leads to the high precipitation seen west of the Rocky Mountains and the Andes.

1.5 Annual Variation in Local Hydrology

Annual variations in the local surface water balance is driven by three main components, precipitation, evaporation, and soil moisture. While the importance of precip-

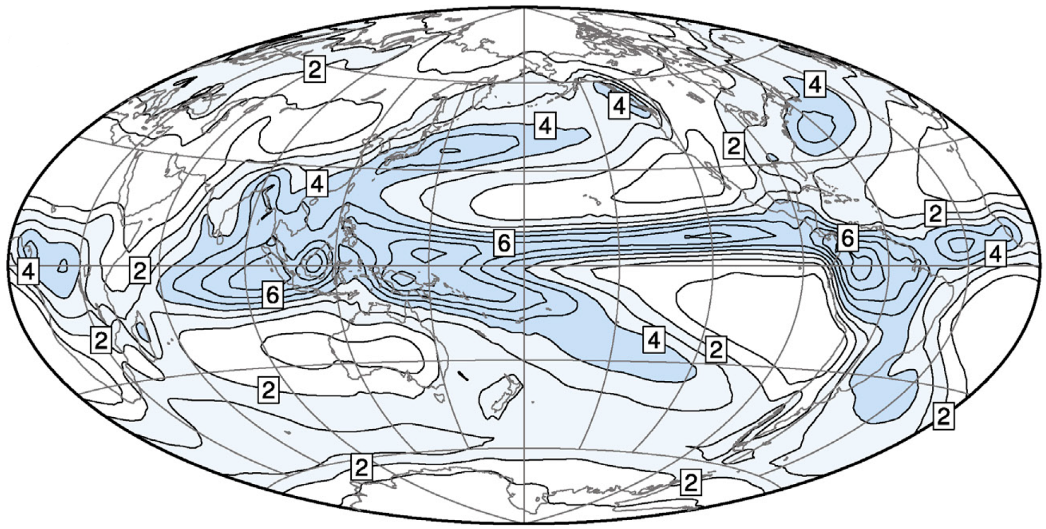

Figure 1.2: Figure 5.4 from Hartmann (2016), showing annual mean global precipitation in millimetres per day, using data from the Global Precipitation Climatology Project.

itation and evaporation is obvious, soil moisture is an important storage component to local water balances. While precipitation is readily observed by most climatological stations, evaporation and soil moisture are less frequently measured (Hartmann, 2016). However, evaporation and soil moisture can be inferred from other readily observed quantities such as temperature and radiation using empirical formulas or models. Another quantity, potential evapotranspiration (PET), can be computed directly from surface radiation, and it captures the evaporation that could occur from sufficiently moist soil. Thus, When PET exceeds evaporation, the soil is generally very dry. For example, figures 1.3a, b, and c show the local water balance for three west coast North American cities in the mid latitudes. All three cities show precipitation peaks during the winter due to strong winter storms. This wintertime peak is stronger for Seattle, which is in the Pacific Northwest and experiences a temperate climate, than San Francisco and Los Angeles in South California which are closer to the equator and experience a more tropical dry climate. The summertime minimum in precipitation increases in duration moving from the Pacific Northwest towards the Southern California locations. In Southern California, the summer minimum corresponds to the highest solar radiation and temperatures and leads to depleted soil moisture, as seen by PET exceeding evaporation from February to November in figures 1.3b and c, and greatly exceeding evaporation from the middle of March to the middle of August. Only in the winter months where temperatures are lowest and precipitation is highest does evaporation exceed PET. Finally, consider Oaxaca, shown in figure 1.3d, which is even closer to the equator in the tropics. High solar radiation and temperatures over the whole year lead to PET exceeding evaporation year-round for Oaxaca, and the strong summer peak in precipitation is associated with the ITCZ and other large scale circulations. Overall, though they are very sensitive to geography, observations and estimation of precipitation, evaporation, and soil moisture (inferred from PET) can provide a good picture of local water balances and the relative wetness or dryness of a location.

1.6 Atmospheric General Circulation and Climate

Phenomena that drive motion and advection in the atmosphere have a large range of temporal and spatial scales. For example, very small-scale phenomena like turbulence, more moderately scaled phenomena like mesoscale (around 10 km to 1000 km) storms,

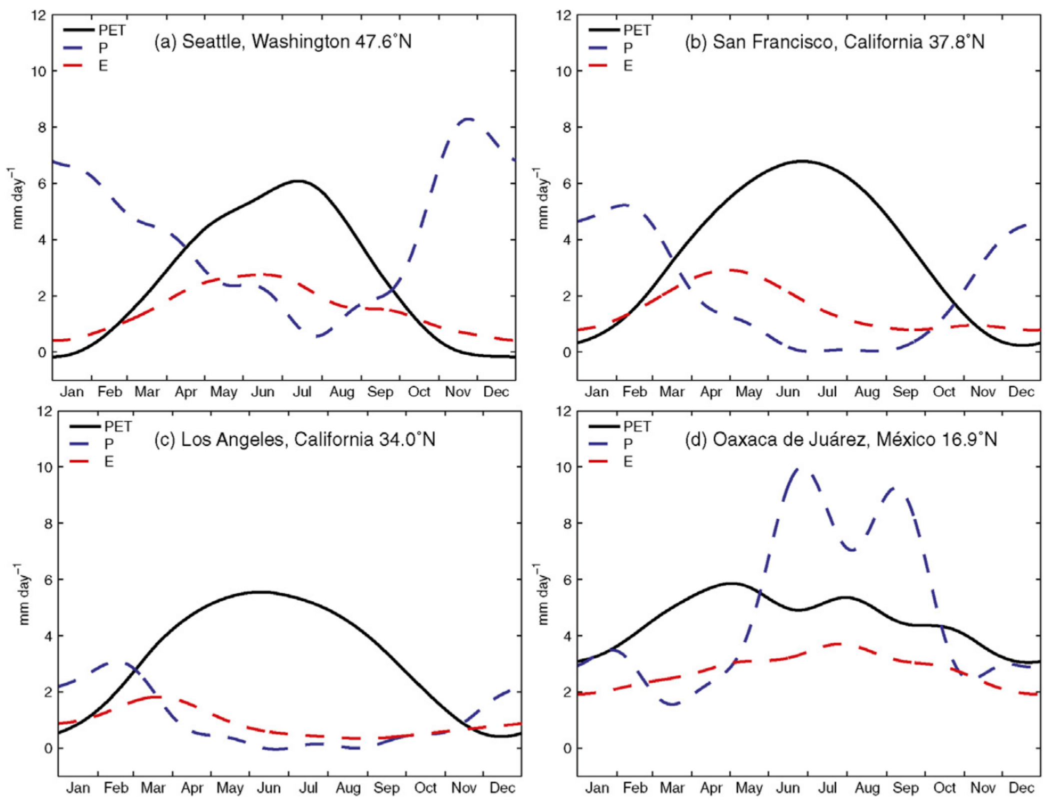

Figure 1.3: Figure 5.6 from Hartmann (2016), showing the annual water balance for four locations, using data the ERA Interim Land Reanalysis data set for 1979–2010 for precipitation (P) and evaporation (E), with estimated potential evapotranspiration (PET).

and parts of large scale phenomena like the rising branches of the Hadley and Ferrel cells can advect moisture and energy vertically into the atmosphere (Hartmann, 2016). Moreover, large-scale phenomena like cyclones and planetary-scale circulations are effective at advecting moisture and energy horizontally over the Earth (Hartmann, 2016). To begin understanding the general circulations in the atmosphere, one can separate the components of wind into horizontal and vertical components. Assuming a spherical Earth with latitude ϕ, longitude λ, and radius a one can define the zonal and meridional components of wind following a parcel with equations 1.5 and 1.6, respectively.

$$u = a\cos(\phi)\frac{D\lambda}{Dt} \tag{1.5}$$

$$v = a\frac{D\phi}{Dt} \tag{1.6}$$

Equations 1.7 and 1.8 give the vertical components of wind in height (z) and pressure (p) coordinates respectively. Equation 1.9 defines the material derivative for an arbitrary quantity y, where $\vec{u} = (u, v, w)$ or $\vec{u} = (u, v, \omega)$ is the flow velocity, and ∇ is the gradient operator.

$$w = \frac{Dz}{Dt} \tag{1.7}$$

$$\omega = \frac{Dp}{Dt} \tag{1.8}$$

$$\frac{Dy}{Dt} = \frac{\partial y}{\partial t} + \vec{u} \cdot \nabla y \tag{1.9}$$

One simplification to more easily understand general circulation over the Earth is by studying zonal averages (means over latitude). The zonal average at a particular latitude for an arbitrary quantity y is given by the square brackets defined by equation

1.10. Zonal averages are useful because many important factors to climate like solar radiation intensity and angular momentum vary with latitude, so locations in the same latitude often share similar climatological features.

$$[y] = \frac{1}{2\pi} \int_0^{2\pi} y d\lambda \tag{1.10}$$

Figure 1.4, taken from Hartmann (2016), shows the zonal mean of zonal wind (eastward wind identified by equation 1.5). Throughout most of the troposphere (below 8 km – 14 km altitude) the zonal wind is westerly, with peak wind speeds above 30 ms^{-1}. These peak speeds are associated with the subtropical jet stream, which is related to the Hadley cell. Air near the equator is at a larger radius from the centre of the Earth than air in the subtropics, thus by conservation of angular momentum air moved from the equator towards the poles will move faster. Thus, the jet streams are fast moving meandering air currents in the atmosphere near the poles and in the subtropics. The subtropical jet stream is located at an altitude of about 12 km and centered near 30° latitude in each hemisphere, and is strongest in the winter season as seen by comparing figures 1.4a and b.

To most easily study the zonal mean meridional and vertical components of wind, one can define a mean meridional mass stream function using equation 1.11 (Hartmann, 2016). The mass stream function can be understood as the flux of mass

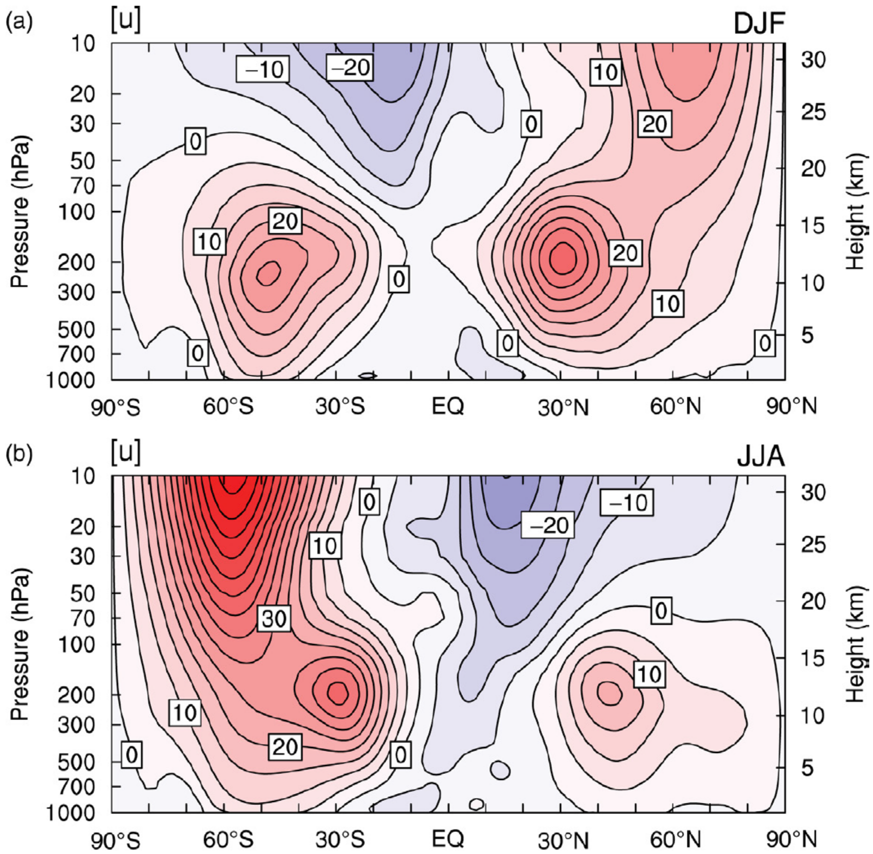

Figure 1.4: Figure 6.4 from Hartmann (2016), showing latitude–height cross-sections of zonally averaged wind speed for the December-January-February months in figure a, and the June-July-August months in b. Contour intervals are at 5 ms^{-1}, westerlies are in red, easterlies are in blue and data is from ERA-Interim.

northward above a specific pressure level p.

$$\Psi_M = \frac{2\pi a \cos(\phi)}{g} \int_0^p [v] dp \tag{1.11}$$

The stream function follows from mass conservation and can be defined for any non-divergent flow. Thus, a useful property of the mass stream function is that the mass flow between any two of its streamlines is equal to the difference between their function values, so the mean meridional velocity and pressure velocity can be related, as shown by equations 1.12 and 1.13.

$$[v] = \frac{g}{2\pi a \cos{(\phi)}} \frac{\partial \Psi_M}{\partial p} \tag{1.12}$$

$$[\omega] = \frac{-g}{2\pi a^2 \cos{(\phi)}} \frac{\partial \Psi_M}{\partial \phi} \tag{1.13}$$

Figure 1.5, from (Hartmann, 2016), shows the annual mean of the mean meridional mass stream function and is a useful tool to visualize two important large scale circulations, the Hadley cell and the Ferrel cells. The Hadley cell clearly dominates the circulation with air rising near the equator, flowing towards the poles in each hemisphere, then sinking in the subtropics. To complete the circulation, the sunk air follows mean meridional winds near the surface to return to the equator. The Ferrel cells circulate in the mid-latitudes with weaker motion and opposite direction. Where the Hadley and Ferrel cells meet is where the subtropical jet occurs. The rising branch of the Ferrel cell raises cold air in the subpolar region, from where it then flows towards equator becoming warmer, before sinking in the subtropics.

While the Hadley cell is a product of uneven solar radiation peaking at the equator, the Ferrel cells are associated with poleward motion generated by eddy circulations. To begin understanding eddies, one can begin with cyclones and anticyclones, which are large wind systems that circulate about a centre point of local pressure anomalies (low pressure for cyclones and high pressure for anticyclones). Cyclones and

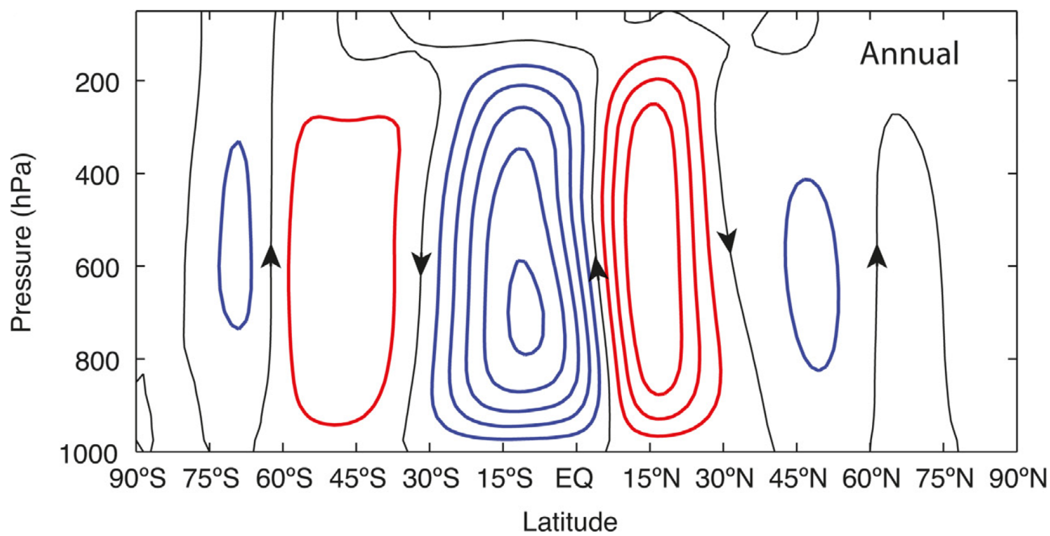

Figure 1.5: Figure 6.5 from Hartmann (2016), showing annual mean of the zonally averaged meridional mass stream function. Contour intervals are 2×10^10 kg s^{-1}, red is positive and blue is negative, with arrows on the zero contours indicating the direction of vertical motion, calculated from ERA-Interim.

anticyclones in the midlatitudes produce significant meridional transport of energy and moisture on the scale of thousands of kilometers. While these fluctuations are not apparent in zonal means, they contribute significantly to zonal mean climate. Fluctuations from a temporal average (indicated with an overbar such as $\bar{y}$) for an arbitrary quantity y can be represented with equation 1.14, while equation 1.15 is a representation of fluctuations from the temporal zonal mean.

$$y' = y - \bar{y} \tag{1.14}$$

$$\bar{y}^* = \bar{y} - [\bar{y}] \tag{1.15}$$

The role of eddies is especially clear when examining heat transport. When northward flowing air is warmer than southward flowing air, northward eddy fluxes of temperature are produced. Thus, the product of meridional velocity and temperature is positive even if the mean meridional wind is zero, allowing equation 1.16 to express the product with a sum (Hartmann, 2016). The three components on the right hand side of equation 1.16 represent contributions from the mean meridional circulation, stationary eddies, and transient eddies, respectively.

$$[\overline{vT}] = [\bar{v}][\bar{T}] + [\bar{v}^{*}\bar{T}^{*}] + [\overline{v'T'}] \tag{1.16}$$

Transient eddies arise from weather disturbances in the mid-latitudes that develop and decay rapidly with temporal scales from a few days to a week. These disturbances generally move eastward following the prevailing winds and contribute significantly to wind and temperature variations which are clearly apparent on weather maps. Eddy fluxes by the time-averaged flow are associated with stationary planetary waves, which are fluctuations of the time average from zonal symmetry. Stationary planetary waves are clearly apparent in monthly mean pressure plots like figure 1.6, taken from Hartmann (2016).

Stationary planetary waves result from the zonal variations in surface topography and temperature associated with continents and oceans. For example, mountain ranges like the Himalayas allow for mechanically forced zonal variation that leads to the peak stationary eddy fluxes in the Northern Hemisphere. Moreover, the

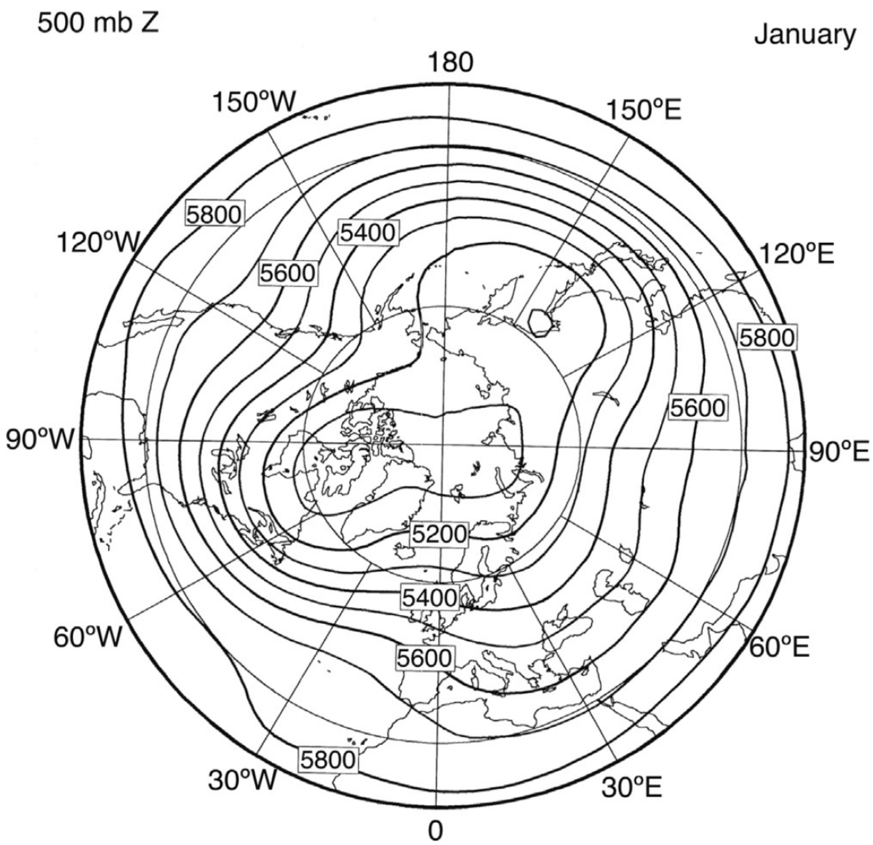

Figure 1.6: Figure 6.8 from Hartmann (2016), showing the average height of the 500 hPa pressure level during January in the Northern Hemisphere, with a 100 m contour interval.

warm Kuroshio and Gulf stream ocean currents contrast with the colder interior temperatures of continents, which allows for thermal forcing that produces stationary planetary waves in the winter. Stationary and transient eddies generate a poleward temperature flux that peaks in the lower troposphere around 50° of latitude in the winter hemisphere. This low altitude peak of the flux is related to the structure of developing cyclones and their peak phase difference between temperature and pressure in the lower troposphere (Hartmann, 2016). The fluxes minimize near the tropopause but then increase with height further into the atmosphere. Seasonal variation in the temperature fluxes is much greater in the Northern Hemisphere than the Southern Hemisphere where there is much more ocean, and thus more stable temperatures due to its high heat capacity. Meridional temperature fluxes are mostly dictated by transient eddies in the Northern Hemisphere, though stationary eddies can contribute about half of the flux in the winter (Hartmann, 2016).

1.7 Dynamical Influences on Extreme Precipitation

Though the Clausius-Clapeyron relationship projects an increase in extreme precipitation intensity, these projections are regionally dependant, as some locations expect a significant increase in extreme precipitation intensity while others expect a decrease (O'Gorman, 2012; Pfahl, O'Gorman, & Fischer, 2017). It is crucial to understand this regional variability to effectively project and ultimately prepare for the potentially destructive effects of extreme precipitation events. Previous work in the field has shown that this regional variability is influenced by changes in the vertical velocity (also known as the ascent) associated with extreme precipitation events (referred to as "extreme ascent") (O'Gorman, 2012; Pfahl, O'Gorman, & Fischer, 2017; Tandon, Zhang, & Sobel, 2018).

Ascent is important to all precipitation events, as it is the way moisture is brought to cooler temperatures higher in the troposphere, where it can condense and precipitate back to the surface. Moreover, while the Clausius-Clapeyron relationship captures the thermodynamic effects on a parcel, ascent captures some of the dynamical effects on a parcel. First consider the basic hydrostatic equation for a parcel at rest, given by equation 1.17, where p is pressure, z is height, ρ is the parcel density, and g is the gravitational constant.

$$\frac{\partial p}{\partial z} = -\rho g \tag{1.17}$$

Equation 1.17 simply states that for a parcel at rest, the vertical pressure gradient force is equal to the gravitational force on the parcel. Now consider a parcel with density ρ' and temperature T' in an environment with density ρ and temperature T. As the parcel, in general, has a different density than the environment, the parcel will displace air in the environment leading to a force of buoyancy. From the hydrostatic equation, the downward gravitational forces on the parcel and the air it displaces are given by $-\rho' g$ and $-\rho g$ respectively. Thus, the net force upward on the parcel is simply the difference between these forces: $g(\rho - \rho')$. We can divide the net force upward by ρ' to find the net buoyant force per unit mass (F_B), as given by equation 1.18.

$$F_B = g\left(\frac{\rho - \rho'}{\rho'}\right) \tag{1.18}$$

By using the ideal gas law ($\rho p = RT$, where R is the ideal gas constant) and noting that both the parcel and the air it displaces experience the same pressure, equation

1.17 can be written in terms of temperature as equation 1.19.

$$F_B = g\left(\frac{T' - T}{T'}\right) \tag{1.19}$$

Both equations 1.18 and 1.19 agree with basic principles as when a parcel is denser than its environment ($\rho' > \rho$) the parcel will sink due to a negative buoyancy force (and vice versa), and when a parcel is cooler than its environment ($T' < T$) it will also sink (and vice versa).

While equation 1.19 is sufficient to capture the effects of temperature on buoyancy for dry parcels, moisture also plays an important role on buoyancy. For example, phase changes in water and their associated latent heat release can affect buoyancy acceleration. Virtual temperature T_v is a quantity that captures some of the effects of moisture in air as it represents the temperature dry air needs to have the same pressure and density as moist air. Virtual temperature is shown in equation 1.20, where R_d is the gas constant for dry air.

$$p = \rho R_d T_v \tag{1.20}$$

Virtual temperature is thus equal to or greater than temperature, usually by a few degrees Celsius. The effects of moisture can be included in equation 1.19 by replacing temperature with virtual temperature to determine the buoyancy force on a parcel more accurately.

These simple relationships of equations 1.18 and 1.19 show that changing temperature under climate change drives precipitation not only through the thermodynamic effects of the Clausius-Clapeyron relationship, but also through the dynamic effects of ascent that lift moisture into the atmosphere. Ascent is also often related to temperature through lapse rates which capture how the temperature of a parcel changes with height.

Ascent via temperature driven buoyancy is a key component of many large scale circulations, such as the Hadley cell. The high solar heat at the equator warms the moist air in that region, decreasing its density so it can ascend into the atmosphere until it is no longer buoyant (due to its density matching that of the environment, for example). This ascent of moist air, due to solar heating, is a cause for the high precipitation typical near the equator. The ascended air then moves poleward as more air warms beneath it. As the warm ascended air is no longer buoyant when it reaches the tropopause, it cannot continue to ascend and instead moves poleward away from the equator. Now closer to the poles, the dry air descends and completes the loop of the circulation by gradually becoming more moist as it follows a return flow near the surface back towards the equator.

Following the reasoning in O'Gorman and Schneider (2009a), the significance of extreme ascent to extreme precipitation intensity can be explicitly shown. Equation 1.21 is the material derivative of moisture in the atmosphere, where q is the specific humidity (the ratio of the mass of water vapor to the total mass of the parcel), e is local evaporation (defined at each point in the atmosphere, in contrast with the vertically integrated evapotranspiration, E, used earlier), and c is local condensation. Equation 1.21 simply relates the change in moisture in the atmosphere (specific humidity q) to its sources (evaporation) and sinks (condensation).

$$\frac{Dq}{Dt} = \frac{\partial y}{\partial t} + \vec{u} \cdot \nabla q + \omega \frac{\partial q}{\partial p} = e - c \tag{1.21}$$

For extreme precipitation events, the ascent term ($\omega \frac{\partial q}{\partial p}$) dominates, and local evaporation is a relatively minor contribution, so equation 1.21 can be simplified to equation 1.22.

$$-\omega \frac{\partial q}{\partial p} \approx c \tag{1.22}$$

Equation 1.23 defines the mass weighted vertical integral for an arbitrary quantity y (the TOA and 0 subscripts indicate the top of the atmosphere and the surface, respectively).

$$\{y\} = \int_{z_0}^{z_{\text{TOA}}} \rho y dz = \frac{1}{g} \int_{p_0}^{p_{\text{TOA}}} y dp \tag{1.23}$$

In height (z) coordinates, equation 1.23 captures changes in density with height. By rearranging and substituting hydrostatic balance (equation 1.17), the height coordinates can be replaced with pressure coordinates (p). Applying 1.23 to equation 1.22, assuming a saturated parcel ($q = q_s$) during the extreme precipitation event, along a moist adiabat (an isopleth of equivalent potential temperature θ^*) converts condensation into precipitation P_e (where the e subscript indicates extreme precipitation) in equation 1.24.

$$\left\{ -\omega \frac{\partial q_s}{\partial p} \right\} \Big|_{\theta^*} = \{c\} = P_e \tag{1.24}$$

As equation 1.24 shows, during extreme precipitation events, the strength of extreme ascent is proportional to the precipitation intensity. Clearly, the dynamical effects of ascent are significant to extreme precipitation intensity regardless of the effects of the Clausius-Clapeyron relationship on buoyancy.

Much previous work on extreme precipitation, such as Tandon, Zhang, and Sobel (2018) and Pfahl, O'Gorman, and Fischer (2017), has attempted to differentiate these dynamical and thermodynamical effects to determine the mechanisms behind the events and their regional variability. Plenty of work, such as Lu et al. (2014) and O'Gorman and Schneider (2009b), has established that these dynamical effects contribute significantly to changes in extreme precipitation events and that, in general, thermodynamical effects are not sufficient to explain the regional changes in extreme precipitation intensity. Indeed, previous work has also shown that extreme precipitation events are typically associated with strong ascent (O'Gorman & Schneider, 2009a). How changes in extreme ascent lead to regional variability in extreme precipitation projections is clear: strengthening extreme ascent favors more precipitation as moisture from the lower troposphere is brought higher into the atmosphere while weakening extreme ascent favors less precipitation (Lu et al., 2014; O'Gorman & Schneider, 2009b; Pfahl, O'Gorman, & Fischer, 2017). Moreover, as explained by O'Gorman (2015), the effects of the dynamical contributions to changes in extreme precipitation intensity are strongest in the tropics and subtropics. As noted by Tandon, Zhang, and Sobel (2018) and Pfahl, O'Gorman, and Fischer (2017), though the greatest source of uncertainty in regional extreme precipitation intensity projections are extreme ascent changes, the reasons behind these changes are still poorly understood.

1.8 The Quasigeostrophic Omega Equation

The quasigeostrophic omega equation is an important theoretical result which expresses vertical velocity at the synoptic scale in relation to key driving mechanisms. Indeed, the quasigeostrophic omega equation has been used as an important analytical tool to study extreme precipitation events through extreme ascent. The quasigeostrophic omega equation is also important where hydrostatic balance is assumed (as in most climate models, as explained in section 1.12) because the standard vertical momentum equation cannot be solved for omega under such conditions. Several assumptions are made to derive the quasigeostrophic omega equation including approximate hydrostatic balance, approximate geostrophic wind (an approximate balance between the Coriolis force and the pressure gradient force), and small Rossby numbers (the ratio of inertia to the Coriolis force is small). The approximate assumptions are why the equation is referred to as "quasi" geostrophic.

Equation 1.25 is a form of the quasigeostrophic omega equation including a diabatic forcing term as shown in Mpanza and Tandon (2022), where p is pressure, σ is the dry static stability, f_0 is a reference value for the Coriolis parameter f, ∇^2 is the horizontal Laplacian operator, R is the ideal gas constant for dry air, ξ is the geostrophic absolute vorticity, Q is the diabatic heating, and Adv is the horizontal geostrophic advection operator shown in equation 1.26. In equation 1.26, u_g is the zonal geostrophic wind while v_g is the meridional geostrophic wind.

$$\partial_{pp}\omega + \frac{\sigma}{f_0^2}\nabla^2\omega = -\frac{1}{f_0}\partial_p \mathrm{Adv}(\xi) - \frac{R}{pf_0^2}\nabla^2 \mathrm{Adv}(T) - \frac{R}{pf_0^2}\nabla^2 Q \tag{1.25}$$

$$\mathrm{Adv}(\cdot) = -u_g\partial_x(\cdot) - v_g\partial_y(\cdot) \tag{1.26}$$

In general, the Laplacian (curvature) of a localized anomaly has opposite sign to the the sign of the anomaly itself. Moreover, the Adv operator behaves similar to a three dimensional Laplacian. These two facts help interpret the terms of the equation. There are three terms on the right hand side of equation 1.25 which can be considered separately. The first term represents forcing from differential vorticity advection. For $\partial_p \mathrm{Adv}(\xi) < 0$, vorticity advection increases with height, which implies that relative vorticity has a greater rate of increase at higher levels in the atmosphere than lower levels. This equivalently implies that the curvature associated with height surfaces has a greater rate of increase at higher levels in the atmosphere than lower levels, so the pressure difference between height levels is decreasing and thus (assuming no other forcing) ascending motion occurs. The second term on the right hand side of equation 1.25 is the Laplacian of temperature advection. If there is spatially localized warm air advection then $\mathrm{Adv}(T) > 0$ and $\nabla^2\mathrm{Adv}(T) < 0$, which implies $\omega < 0$, in the absence of other forcings. The third term on the right hand side of equation 1.25 is the diabatic heating term and is mostly associated with convective heating on the temporal scale of an extreme precipitation event. For a positive localized convective heating anomaly, $\nabla^2 Q < 0$, and so the convection forces ascent. Static stability, σ, is the key parameter on the left hand side of equation 1.25 as for a given positive forcing a smaller σ value implies less atmospheric stability and thus larger values of ω.

Following the reasoning of Nie and Sobel (2016) and Mpanza and Tandon (2022), by assuming a wavelike structure for ω with horizontal length scale L during extreme precipitation events, the Laplacian in equation 1.25 can be replaced with $-1/L^2$ yielding equation 1.27 (where E indicates values during extreme precipitation events).

$$\partial_{pp}\omega_E - \frac{\sigma\omega_E}{f_0^2 L_E^2} = -\frac{1}{f_0}\partial_p \mathrm{Adv}(\xi_E) + \frac{R}{p f_0^2 L_E^2}\mathrm{Adv}(T_E) + \frac{R Q_E}{p f_0^2 L_E^2} \tag{1.27}$$

Through scaling analysis, Nie and Sobel (2016) showed that the Rossby radius of deformation, L_R, is a useful scale for determining the dominant balances in equation

1.27, introducing two regimes of study: large eddy lengths scales where $L_E > L_R$ and small eddy length scales where $L_E < L_R$. Nie and Sobel (2016) show that for large eddy lengths where $L_E > L_R$, the first term on the left hand side and the first term on the right hand side dominate the balance, indicating that large scale circulation decouples from convection and so ascent is determined entirely by the differential vorticity advection. Under such conditions, increasing eddy lengths are expected to lengthen the advective time scale of a precipitation system thus increasing the event's accumulated precipitation (Dwyer & O'Gorman, 2017). Correspondingly, for small eddy lengths where $L_E < L_R$, convection and large-scale circulation are strongly coupled so adiabatic ascent, temperature advection, and diabatic heating dominant the balance (Nie & Sobel, 2016). Tandon, Zhang, and Sobel (2018) provide evidence that suggests extreme ascent changes in the subtropics projected in global climate models are mostly driven by changes in diabatic heating, which follows from subtropical L_E being smaller than L_R and suggests that contributions from differential vorticity advection are weak. Under such conditions, increasing eddy length is expected to reduce coupling between convection and large scale circulation and thus lead to weakening extreme ascent. Much of this analysis shows that the coupling strength between convection and large scale circulation determines much of the influence of eddy length on precipitation. Under strong coupling, increasing L_E is expected to decrease extreme precipitation intensity, while under weak coupling increasing L_E is expected to have the opposite effect and increase extreme precipitation intensity.

1.9 The Horizontal Scale of Ascent

Recent work has analysed several potential drivers of extreme ascent changes. For example, Tandon, Zhang, and Sobel (2018) suggest that changes in extreme ascent are likely a result of changes in the horizontal scale of ascent. On the other hand, Li and O'Gorman (2020) suggest that vertical stability changes may contribute significantly to extreme ascent changes. Furthermore, Mpanza and Tandon (2022) suggest that changes in differential vorticity advection play a key role in extreme ascent and extreme precipitation intensity changes. Clearly, there may be several mechanisms that drive extreme ascent changes and their relative contributions may differ by region or season. In this section we focus on the mechanisms described by Tandon, Zhang, and Sobel (2018), as it provides a theoretical justification to study the horizontal scales of extreme precipitation events in this thesis. Furthermore, spatial scales (along with temporal scales) are fundamental features of all precipitating weather systems, so studying them can provide important insight beyond their potential contributions to extreme ascent.

Tandon, Zhang, and Sobel (2018) provides a theoretical explanation for changes in the dynamical part of extreme precipitation, extreme ascent, using the quasi-geostrophic omega equation, which expresses vertical velocity at the synoptic scale. Tandon, Zhang, and Sobel (2018) begin with equation 1.27 and apply thermal wind balance to simplify the right hand side terms in terms of the characteristic scales of height, horizontal velocity, and anomalous horizontal temperature gradient. By considering typical values for diabatic heating, the characteristic scale of horizontal velocity, and the Coriolis parameter, Tandon, Zhang, and Sobel (2018) show that horizontal advection terms are expected to have relatively minor contributions to vertical velocity anomalies, producing equation 1.28.

$$L_E^2 \partial_{pp} \omega_E - \frac{N_E^2 \omega_E}{f^2} = \frac{R Q_E}{p f^2} \tag{1.28}$$

If ω_E vanishes at the top and bottom of the troposphere and is parabolic over the depth of the troposphere, then ω_E has a unique representation related to the extreme ascent at a representative level within the troposphere, given by equation 1.29, where ω_e is the extreme ascent at a representative level within the troposphere, p_t is the pressure at the tropopause, p_s is the pressure at the surface, and p_m is the pressure at a representative level within the troposphere (Tandon, Zhang, & Sobel, 2018).

$$\omega_E = \omega_e \frac{(p - p_t)(p_s - p)}{(p_m - p_t)(p_s - p_m)} \tag{1.29}$$

Evaluating equation 1.28 at the representative pressure level and applying equation 1.29 yields a model for extreme ascent in equation 1.30, where Q_e is the diabatic heating anomaly, H_p is the pressure depth of the troposphere, R is the gas constant for dry air, N_e^2 is the dry stability, and L_e is the horizontal scale of ascending anomalies.

$$-\left[\frac{2H_p^2L_e^2}{(p_m-p_t)(p_s-p_m)}+\frac{N_e^2H_p^2}{f^2}\right]\omega_e=\frac{RH_p^2Q_e}{p_mf^2} \tag{1.30}$$

After simplifying equation 1.30 under the relevant conditions, climate change perturbations in extreme ascent can be expressed with equation 1.31, where the 0 subsript indicates the original value of the quantity.

$$\frac{\delta\omega_e}{\omega_{e0}}\approx\frac{\delta L_e^2}{L_{e0}^2}-\frac{\delta Q_e}{Q_{e0}} \tag{1.31}$$

By studying the components of equation 1.31 using models, Tandon, Zhang, and Sobel (2018) showed that changes in extreme ascent and the horizontal scale of ascent have similar spatial structure, with increases in the horizontal scale corresponding with weakening ascent, as equation 1.31 predicts. Moreover, their analysis shows that changes in the horizontal scale and diabatic heating together account for most of the changes in ascent, though there may be other effects too.

While studying changes in the horizontal scale of ascent as a projection tool of extreme precipitation intensities justifies this thesis, Tandon, Zhang, and Sobel (2018) also provide an explanation for the changes in horizontal scale of ascent, by first relating the horizontal scale of extreme ascent to the horizontal scale of atmospheric eddies (which were introduced in section 1.6). Eddy length scales should in turn be dictated by the Rossby radius of deformation, as it is the scale at which eddy generating cyclones and anticyclones occur. Finally, the Rossby radius of deformation itself is proportional to dry stability. However, though there have been global increases in dry stability and eddy length scales, there very clearly have not been corresponding global increases in the horizontal scale of extreme ascent, and thus the relationship cannot hold as proposed (Kidston et al., 2010). To correct this relationship, Tandon, Zhang, and Sobel (2018) suggest accounting for latent heat release associated with moisture, which is plausible because moist parcels experience less stability than dry parcels because moisture condensation and latent heat release leads to further ascent for moist parcels if they are surrounded by cool air. Tandon, Zhang, and Sobel (2018) account for this moisture effect by modifying dry stability to capture latent heat release on moist adiabats when the parcel is above a 98% relative humidity threshold. This modified version of dry stability is introduced as "effective stability". Further modelling results show that changes in the horizontal scale of extreme ascent more closely correspond to changes in effective stability than dry stability, implying that effective stability may drive changes in the horizontal scale of ascent. However, the causality of which quantity induces the other is not necessarily clear everywhere. Regardless, Tandon, Zhang, and Sobel (2018) are able to identify a more complete chain of causality relating climate change to decreases in extreme precipitation intensity in the subtropics: decreases in stability lead to a decrease in the horizontal scale of ascent, which leads to stronger extreme ascent and extreme precipitation intensity.

1.10 Temporal Scales of Extreme Precipitation Events

While this thesis primarily focuses on the spatial scale of extreme precipitation events and how they relate to intensity under climate change, temporal scales also influence extreme precipitation intensity. The relationship between time scales and spatial scales can be considered using equation 1.32 from Dwyer and O'Gorman (2017), where τ is the advective time scale, L is the zonal length of the event, U is the absolute value of the time-averaged zonal wind at a nominal steering level for storms, and $U_0 = 5$ m s^{-1} is an offset that represents meridional velocities, eddy zonal velocities, and internal storm dynamics. (In practice, U_0 prevents an unphysically long time scales in regions where mean zonal wind is weak.) Equation 1.32 is a simplified expression that aims to primarily capture one of the most important factors in midlatitude precipitation duration, the advective influence of large-scale mean flow (Dwyer & O'Gorman, 2017).

$$\tau = \frac{L}{U + U_0} \tag{1.32}$$

As shown by equation 1.32, both the zonal wind and the zonal length associated with an extreme precipitation event can affect its time scale. Most simply, 1.32 shows a proportionality between time scale and spatial scale, but the zonal wind terms play an important role. For example, due to sea ice loss, the Arctic is warming faster than the rest of the planet, leading to a weakening meridional temperature gradient and thus weaker zonal wind, following from thermal wind balance. Assuming fixed spatial scales, weaker zonal wind would be expected increase event duration. However, zonal winds are affected by changes in other temperature gradients and shifts in eddies and spatial scales have been shown to change so the effect is not consistent over the entire planet. Importantly, previous work with climate models (including Dwyer and O'Gorman (2017)) and convection-permitting models has shown that changes in extreme precipitation duration are small compared to changes in intensity, and thus this thesis and many other studies have focused primarily upon studying changes in intensities and spatial scales (Chan et al., 2016; Dwyer & O'Gorman, 2017; Kao & Ganguly, 2011).

1.11 IDF Curves

Three important quantities can describe a precipitation event for a certain location: intensity, duration, and frequency. The intensity of a precipitation event refers to the rate of precipitation, usually given as mm hr^{-1} for various times over the duration of an event. The duration of a precipitation event is the period of time over which a precipitation event is studied. Duration may also refer to the total lifetime of a precipitation event under some given definition. Finally, the frequency of an event refers to the frequency at which such an event would occur in time, such as once every year or once every 20 years, and is closely related to the concept of a return period. The period of time between which a certain kind of precipitation event is expected to repeat is referred to as the return period.

An intensity-duration-frequency (IDF) curve summarizes this information in a graph using rainfall observations, such as the IDF curve given in figure 1.7. There are several curves in figure 1.7 corresponding to various return periods, as indicated on the bottom right hand side of the plot. Curves corresponding to longer return periods thus correspond to rarer events. As one may expect, rarer events correspond to greater intensity. IDF curves are frequently used in engineering fields such as architecture or urban planning where knowledge of the intensity and rarity of precipitation events is used to justify structural decisions, for example.

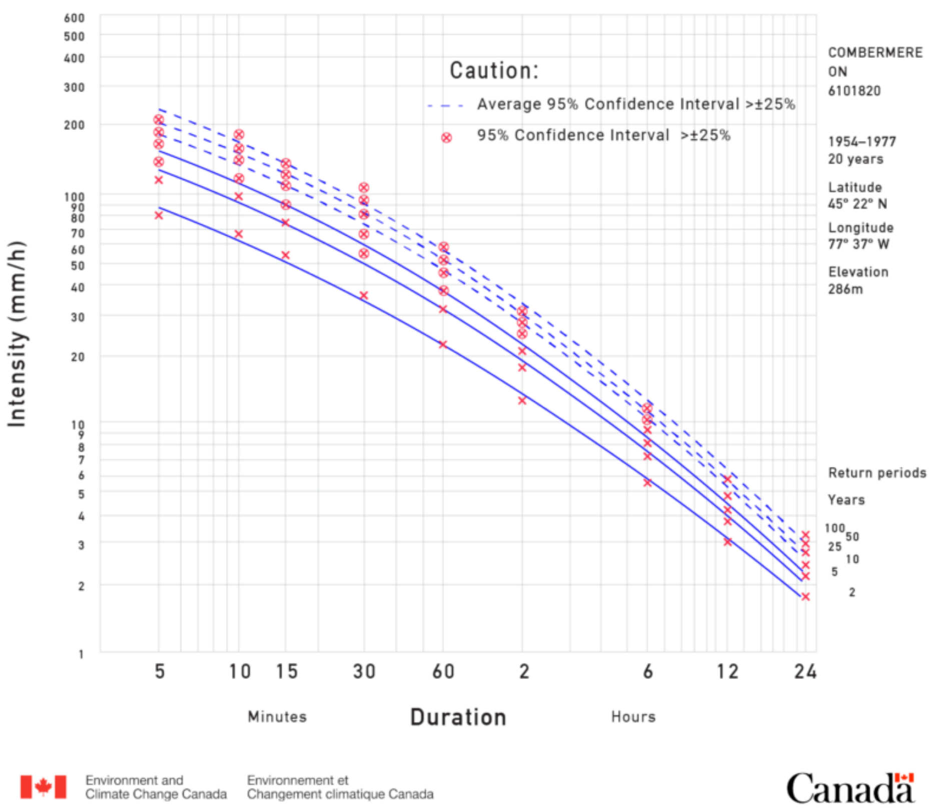

Figure 1.7: A sample IDF curve from Environment and Climate Change Canada for a location in Ontario from 1954 to 1977 (“IDF Curve”, n.d.).

As IDF curves are based on observations, they usually include information to describe uncertainty, such as confidence intervals. The IDF curve in figure 1.7 is from Environment and Climate Change Canada and represents confidence intervals in a specific way. Solid lines and crosses indicate that the 95% confidence interval for that curve or point is less than 25% of the central value, so the confidence interval is very narrow and thus the uncertainty is relatively low. Dashed lines and circled crosses indicate curves or points where the 95% is more than 25% of the central value, so the confidence interval is wide and thus the uncertainty is relatively high.

1.12 The Atmosphere in Climate Models

A climate model is essentially a computer program that can simulate the climate of the Earth by incorporating the relevant mathematical formulations of physics, chemistry, and biology. Climate models themselves are often categorized into global climate models and earth system models. Earth system models are like global climate models, but they often involve more complex methods to account for features of the Earth that can change in response to a changing climate, such as vegetation, the carbon cycle, or atmospheric chemistry.

The atmospheric component of a global climate model includes a spatial grid that represents locations over the Earth and a vertical grid that represents the layers of the atmosphere. Most climate models have a horizontal resolution between 25 km and 500 km, and around 35 to 50 vertical levels. In contrast, weather prediction models that aim to produce forecasts ten days in the future currently have about a 15 km horizontal resolution and around 150 vertical levels (Hartmann, 2016). Weather models are also usually run over limited domains rather than global domains. While horizontal grids are usually equally spaced (in degrees or in kilometers), vertical grids usually are not because the highest resolutions are usually needed where complex effects are common, such as near the lower boundary for turbulence, and the tropopause for stratosphere-troposphere transport. While degrees or kilometers can be used as the horizontal coordinates of a climate model's grid, surface normalized pressure (referred to as the "sigma coordinate system") is often used as the vertical coordinate because it can inherently include topographical features, which makes it easy to conserve mass in the models. Computational cost is the main bottleneck to higher resolution climate models and so they are sometimes run at lower resolution when producing climate simulations.

The most basic atmospheric dynamics of a climate model are described using conservation equations for fluids such as those for momentum, mass, or energy. There is also special care given to water conservation in climate models, as water vapour has a significant effect on many climate phenomena (Hartmann, 2016). As is often the case in practical physics, climate models simplify the full equations into primitive equations to neglect insignificant effects, such as the oblateness of the Earth. Climate models are also simplified based on several common assumptions. For example, hydrostatic balance is assumed in most climate models so that the vertical pressure gradient force is equal to the force of gravity. Another assumption takes the gravitational acceleration in the atmosphere as constant, which follows from the atmosphere being much thinner than the radius of the earth. Moreover, the grid scale resolution of a model is often too coarse to simulate the phenomena associated with the sources and sinks of conserved quantities, such as momentum and heat. Such phenomena are described as "sub-grid-scale" and their effects are realized in climate models by inferring them from phenomena and quantities that are simulated at the grid scale in a process known as "parameterization." Several key phenomena such as radiation, convection, and turbulence are parameterized in global climate models and thus the general behavior of climate models are strongly influenced by their parameterization processes.

Radiative transfer is of obvious importance to climate models as it captures the relationship between solar heating from the sun and infrared cooling towards space, one of the main energy components of the Earth's climate. Despite this importance, radiative transfer is parameterized in models to generally accurate effect (Hartmann, 2016). For example, rather than explicitly simulating the interactions between solar radiation and the chemical components of clouds, some models treat clouds to be horizontally homogeneous across a grid cell. Parameterized features of clouds can include cloud cover and their optical properties, which themselves can have some fixed seasonal variation.

Convection is also parameterized in models, and is closely associated with clouds.

Interestingly, vertical advection associated with parameterized sub grid scale convection is often stronger than that associated with large scale flow realized at the grid level. The goal of convection and cloud parameterization in models is in large part to resolve the discrepancy between the grid level resolution of climate models with the much smaller spatial scales of convection and clouds. Cloud and convection parameterization processes in climate models try to account for at least three significant effects: water vapour condensation and the effects of latent heat, vertical advection associated with clouds, and interactions between cloud particles and radiation (Hartmann, 2016). The Hadley cell, for example, is driven by latent heat release during intense convection, so realistic coupling between climate model convection and large-scale flows is critical to accurately simulate the climate.

An example of a convective parameterization is the "moist adiabatic adjustment". A model using this parameterization first checks if the lapse rate has exceeded the moist adiabatic lapse rate (~ 6.5 K km^{-1}) in a vertical layer. If so, the heat and moisture of the vertical layer is readjusted to: make the lapse rate equal to the moist adiabatic lapse rate, conserve energy, and "rain out" (realize as precipitation) any excess moisture. This is unrealistic because the entire grid box is treated like a convective element though in reality convection occurs at a much smaller spatial scale. In some modern models, such as CAM6 (the atmospheric component of the CESM2 model), there are schemes that attempt to parameterize plumes rather than treating the whole grid box like a convective element ("CAM6 Scientific Guide", 2017).

2 | Methods

2.1 Defining EPEs and Dataset Considerations

All of the model output used in this analysis were from the Coupled Model Intercomparison Project Phase 6 (CMIP6) (Eyring et al., 2016), with some from the CMIP6 sub-project, HighResMIP (Haarsma et al., 2016). CMIP is an international collaboration among modelling centres to allow for the intercomparison of global climate models by producing output from all the participating models under a standardized set of climate scenarios. CMIP model output has contributed to many internationally recognized endeavours, such as the IPCC reports. CMIP model output is also readily available for download and use by scientists on the Earth System Grid Foundation's online archive. As the name suggests, the HighResMIP sub-project specifically focuses on high resolution climate models.

EPEs can be defined in several ways. For example, some earlier studies (e.g., O'Gorman & Schneider, 2009b) used a percentile threshold to define extreme precipitation events, such as only the top 0.1% events within the study period. For this analysis, a return period approach was used. A return period is the time period over which the extreme event is identified. For example, a once in 50-years event corresponds to a 50-year return period, while a once per year event corresponds to a one-year return period. For this analysis, a one-year return period was used with an EPE defined as the event in the return period with the maximum daily accumulated precipitation, for each location. Annual maxima correspond approximately to a 99.7% percentile threshold for daily precipitation. A one year return period was used to allow for sufficient sampling of the events in the 20-year study period from 1981 to 2000, and this is a common approach in earlier studies (e.g., Pfahl, O'Gorman, & Fischer, 2017; Tandon, Zhang, & Sobel, 2018). Thus, in each model, each location provides one EPE per year, for 20 total EPEs. The 1981 to 2000 study period was used to allow for comparison with previous work in the field (e.g., Pfahl, O'Gorman, & Fischer, 2017; Tandon, Zhang, & Sobel, 2018).

In this analysis, five quantities available from CMIP6 were used (variable name in the CMIP6 archive given in brackets): vertical velocity (wap), precipitation (pr), grid scale precipitation (prl), parameterized convective precipitation (prc), and geopotential (zg). CMIP6 only has prc available, so prl is computed as the difference of pr and prc. Vertical velocity and geopotential were analyzed at the 500 hPa pressure level. This level was chosen because pressure levels closer to the surface included too many topographical features, while pressure levels at higher altitudes did not capture the dynamical effect this analysis aims to study. Unless otherwise stated, all computation were performed using model output at daily resolution because many models did not report data at higher temporal resolution. However, we will show results of sensitivity tests to demonstrate that our results were not sensitive to the choice of temporal resolution. Table 2.2 gives an overview of the included models and their available quantities for this analysis, as not all models archived all of the required quantities for our analysis.

Precipitation length scales were also computed for three satellite-based observational data sets: CMORPH (Xie et al., 2019), IMERG (Huffman et al., 2019), and CPCP V3.2 (Huffman et al., 2022). CMORPH is an algorithm that uses observations from passive microwave measurements on low earth orbit satellites and infrared brightness temperature data from geostationary instruments. CMORPH provides a flexible technique through which estimates from existing microwave rainfall algorithms can be combined (Xie et al., 2019). CMORPH data is on an 8 km $\times$ 8 km grid over a global domain from 60°S to 60°N, with temporal resolution up to 30 minute intervals from January 1, 1998 to the present. IMERG is an algorithm that uses NASA and JAXA's GPM (Global Precipitation Measurement) satellite constellation to produce a precipitation dataset. IMERG data is on a $0.1^\circ \times 0.1^\circ$ grid over a full global domain, with temporal resolution up to 30 minute intervals intervals from June of 2000 to the present. GPCP is an algorithm that uses input from the same satellites as IMERG to produce a dataset on a $0.5^\circ \times 0.5^\circ$ grid over a full global domain with daily temporal resolution from June of 2000 to the present. While these three datasets are distinct products, they incorporate each other somewhat as GPCP V3.2 uses IMERG as an input in the 55°N to 55°S latitude range (Huffman et al., 2022) and CMORPH uses GPCP for bias correction over the ocean (Xie et al., 2019). CMORPH only provides coverage in the 60°N to 60°S latitude range, while GPCP and IMERG provide global coverage. CMORPH's truncated spatial coverage was inconsequential as this analysis focused on the 55°s to 40°S latitude range. All three observational data sets provide data at daily temporal resolution or higher, which matched the models' temporal resolution. These datasets are also distinct from reanalysis data products which use models and observations to produce data products. We did not consider reanalysis products in this study as they provided an overlap with the model results from CMIP6. Though the model datasets used were from 1981 to 2000, an additional sensitivity test (shown in the results section) showed that extreme precipitation length scale means from the models computed from 1981 to 2000 differed little from those computed from 2000 to 2014 (historical model output past 2014 is not yet available in CMIP6). Thus, model results from 1981 to 2000 can be reasonably compared with observational results from 2000 to 2014.

2.2 Computing Horizontal Scales

Horizontal scales were computed following the method of Tandon, Zhang, and Sobel (2018), as follows:

1. For each grid cell for each model, the day of maximum precipitation (the "an-

nual maximum") is determined for each year in the study period. To compute anomalies, we subtract from the full field the climatology field.

2. The horizontal scale for each annual maximum is computed by first determining the e-folding distance of the relevant quantity's anomaly in each cardinal direction. The e-folding distance is the distance away from the cell of study at which the relevant quantity's anomaly decreases by a factor of e.

3. The east and west e-folding distances are averaged to determine a zonal e-folding distance, and the north and south e-folding distances are averaged to determine a meridional e-folding distance.

4. The zonal and meridional e-folding distances are then scaled by dividing them by $0.19 \times 2\pi$ to determine their scales in the standard inverse wavenumber form. This scaling follows Barnes and Hartmann (2012), as the e-folding distance of a cosine wave is 0.19 times its wavelength.

5. the zonal and meridional wave numbers are combined with a Euclidean norm to determine a combined horizontal scale of the quantity,

$$L = \left[(L_x^{-2} + L_y^{-2}) \right]^{-\frac{1}{2}} \tag{2.1}$$

where L is the horizontal scale, and L_x and L_y are the zonal and meridional inverse wave numbers, respectively.

This computation is repeated for each grid cell, for each year in the study period, for each model, for each quantity. The horizontal scales for each quantity are then averaged over the study period for each grid cell, for each model. This computation was also followed to produce length scales from the observational precipitation data sets.

In step 1 the annual maxima were determined for each model or observational data set individually as the day of maximum precipitation in one data set is not necessarily the same as in another data set. The climatology field used in step 1 is computed from the monthly mean of the quantity over the entire epoch (1981 to 2000). To determine the e-folding distance as in step 2 in the east direction, for example, the anomalies of the adjacent cells are checked, moving eastward, until a cell with an anomaly below the e-folding value is reached. After reaching this e-folding value, the distance between the cell of study and the cell with the e-folding value is summed, using linear interpolation between the last two cells to determine the e-folding distance. North and south e-folding distances over the poles were computed by following a straight line over the pole. For example, following the 30°W longitude line northward before the north pole would lead to following the 150°E longitude line southward once the pole was crossed. For events whose computed zonal or meridional length scale is below the model grid spacing, the length scale is set to the model grid spacing. This adjustment has no significant effect on our results, as almost all EPEs in all models have spatial scales greater than the model resolution.

Figure 2.1 shows a typical plot of L_x and L_y away from a cell of study for the vertical velocity anomaly during an EPE. Notice that at a distance of L_y south of the cell of study the vertical velocity anomaly has not reached the e-folding value but a distance L_y north of the cell of study the the e-folding value has been reached. Similarly, the e-folding value is reached L_x east of the cell of study, but not west of the cell of study. This behaviour is typical due to averaging the e-folding distance zonally and meridionally before computing L_x and L_y, respectively.

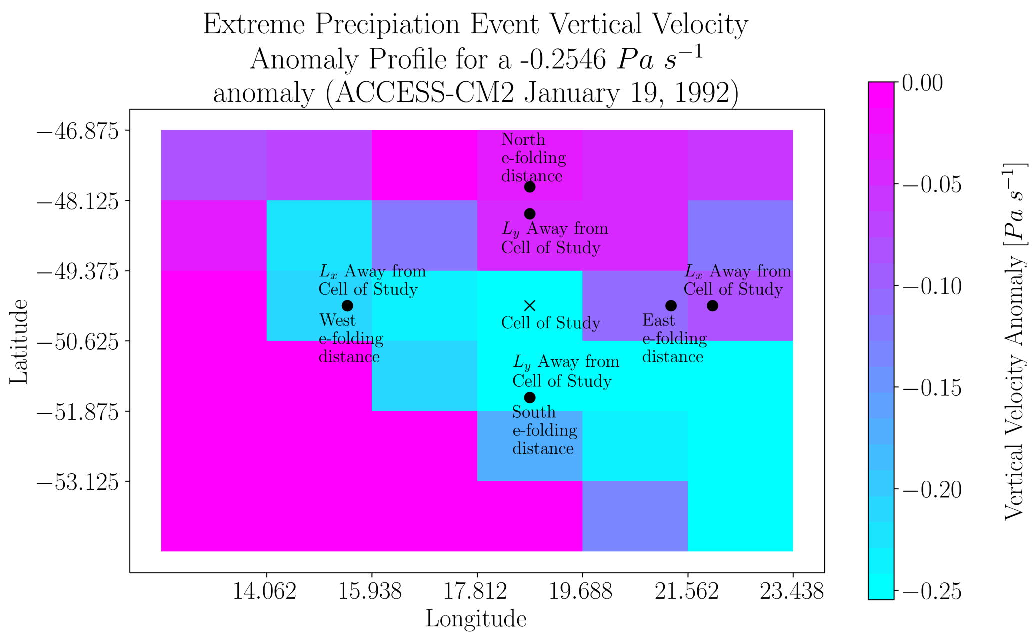

Figure 2.1: A plot showing points that are a distance of L_x and L_y from the cell of study, and e-folding distances for all four cardinal directions, for the vertical velocity anomaly during a typical EPE in the ACCESS-CM2 model. The centre of the cell of study is indicated with an X symbol, while dots correspond to distances away from the cell of study. Some dots also overlap due to closeness.

There are other approaches for computing spatial scales that might be suitable in particular situations. For example, a long narrow storm system with a northeastward orientation, such as those that can occur in a mesoscale convective system, would have a spatial structure better described by length scales oriented along the northeastward axis of the storm system rather then length scales oriented along the cardinal directions. Our approach for computing spatial scales is not meant to account for every possible storm structure, but is rather meant to provide a standard characterization of storm structure that facilitates physical analysis and comparison with earlier studies. For instance, wavelike disturbances fed into the standard form of the QG omega equation would produce wavenumbers in the cardinal directions. One alternative approach is the Fourier decomposition approach used by Kidston et al. (2010), in which a quantity is first decomposed into Fourier components around latitude circles. The Fourier components are then converted to wavenumbers and averaged, before the mean wavenumber is converted to a wavelength that represents a length scale. While this approach has been successful, spatially narrow storms produce a broad range of wavenumbers which can create ambiguity about the spatial scale of the quantity. In contrast, the e-folding approach used here computes the length scale directly from the physical extent of the anomaly. Moreover, historical values of the horizontal scale computed from the e-folding approach correspond well with the eddy length scale computed using the Fourier method of Kidston et al. (2010) (Barnes & Hartmann, 2012; Tandon, Zhang, & Sobel, 2018).

For all quantities except for geopotential, all anomalies were of one sign (they were either all positive or all negative). During precipitation events low pressure in the lower troposphere is accompanied by high pressure in the upper troposphere. The 500 hpa pressure level is in the middle of the troposphere, so depending on the vertical structure of a storm the location of the 500 hpa level may change, leading to both positive and negative geopotential anomalies. For geopotential during extreme precipitation events, significant numbers of both positive and negative anomalies occurred, so horizontal scales were computed for both kinds of anomalies. Moreover, the results from just the negative anomalies were very similar to those using both kinds of anomalies.

Table 2.1: A summary of all the CMIP6 models and quantities included in this analysis. Quantities are referred to by their CMIP6 variable name (wap, pr, prl, prc, and zg are vertical velocity, precipitation, grid scale precipitation, convective parameterized precipitation, and geopotential, respectively). We used output from the "historical" scenario for all CMIP6 models and the "hist-1950" scenario for all HighResMIP models.

Model Name	**CMIP Activity**	**Resolution (Cells)**		**Nominal**	**Quantity**			
		Latitude	Longitude	**Resolution (km)**	wap	pr	prc	zg
ACCESS-CM2	CMIP	144	192	250	X	X	X	X
BCC-CSM2-HR	HighResMIP	400	800	50	X	X	X	
CanESM5	CMIP	64	128	500	X	X	X	X
CESM2	CMIP	192	288	100	X	X	X	X
CESM2-FV2	CMIP	96	144	250	X	X	X	X
CESM2-WACCM	CMIP	192	288	100	X	X	X	X
CESM2-WACCM-FV2	CMIP	96	144	250	X	X	X	X
CMCC-CM2-HR4	HighResMIP	192	288	100	X	X	X	
CMCC-CM2-VHR4	HighResMIP	768	1152	25	X	X		
EC-Earth3	CMIP	256	512	100	X	X	X	X
ECMWF-IFS-HR	HighResMIP	361	720	25	X	X	X	
ECMWF-IFS-LR	HighResMIP	181	360	50	X	X	X	
ECMWF-IFS-MR	HighResMIP	181	360	50	X	X	X	
GFDL-CM4	CMIP	90	144	250	X	X		X
HadGEM3-GC31-HH	HighResMIP	768	1024	50	X	X	X	
HadGEM3-GC31-HM	HighResMIP	768	1024	50	X	X	X	
HadGEM3-GC31-LL	HighResMIP	144	192	250	X	X	X	
HadGEM3-GC31-MM	HighResMIP	324	432	100	X	X	X	
HiRAM-SIT-HR	HighResMIP	768	1536	25	X	X	X	
IITM-ESM	CMIP	94	192	250	X	X	X	X
INM-CM4-8	CMIP	120	180	100	X	X	X	X
INM-CM5-0	CMIP	120	180	100	X	X	X	X
MPI-ESM-1-2-HAM	CMIP	96	192	250	X	X	X	X
MPI-ESM1-2-HR	HighResMIP	192	384	100	X	X	X	X
MPI-ESM1-2-LR	CMIP	96	192	250	X	X	X	X
MPI-ESM1-2-XR	HighResMIP	384	768	50	X	X	X	
TaiESM1	CMIP	192	288	100	X	X	X	X

3 | Results

3.1 Horizontal Scales of Extreme Ascent

To begin investigating the relationship between model resolution and the computed length scales, typical global plots of the models' vertical velocity length scales can first be investigated for general behaviour. As explained in the introduction, changes in extreme ascent length scales are a likely driver of extreme precipitation intensity changes, so it is a natural quantity to begin studying the length scales of EPEs. Figures 3.1a, b, and c are plots for the CanESM5, EC-Earth3, and HiRAM-SIT-HR models, respectively. All the models appear to have similar meridional structure with peak vertical velocity length scales at the poles, with more local peaks near the equator. Other spatial similarities between the models include various local peaks such as the west coasts of North America, South America, and Africa in the subtropics. The models also all follow similar behaviour where the length scales over the ocean are generally greater than those over land. Moreover, the models do not show any simple correspondence between extreme ascent strength and extreme ascent length scales, as noted in previous studies such as (Tandon, Zhang, & Sobel, 2018). For example, length scales are generally large in both the subtropical dry zones and the extratropical regions, but extreme ascent is generally weakest in the subtropical dry zones and strong in the extratropical regions (Tandon, Zhang, & Sobel, 2018). The average magnitude of the length scales differs between the models, for example the global mean length scales for the CanESM5, EC-Earth3, and HiRAM-SIT-HR models are around 265 km, 204 km, and 269 km, respectively. This apparent spread in length scale magnitudes motivates further investigation into the differences between the models.

How do the models' vertical velocity length scales behave, and differ in the zonal average? From figure 3.2 the latitude dependence of the models is clear with local maxima near the poles and the equator, and other local maxima in the subtropics and midlatitudes. Additional analysis (not shown) showed that the maxima near the poles was mostly due to drizzle effects inflating the length scales in that region. For example, many EPEs near the poles have precipitation close to zero, so the e-folding distance for quantities around the EPE are inflated as the other grid cells around the EPE will have precipitation values that are also already close to zero. This may also be true in the subtropics where extreme precipitation intensity is low, but more work is needed to check this. In contrast, an EPE closer to the equator will have high precipitation such that more typical precipitation values in grid cells away from the EPE will be well below the e-folding value, leading to e-folding distances smaller than

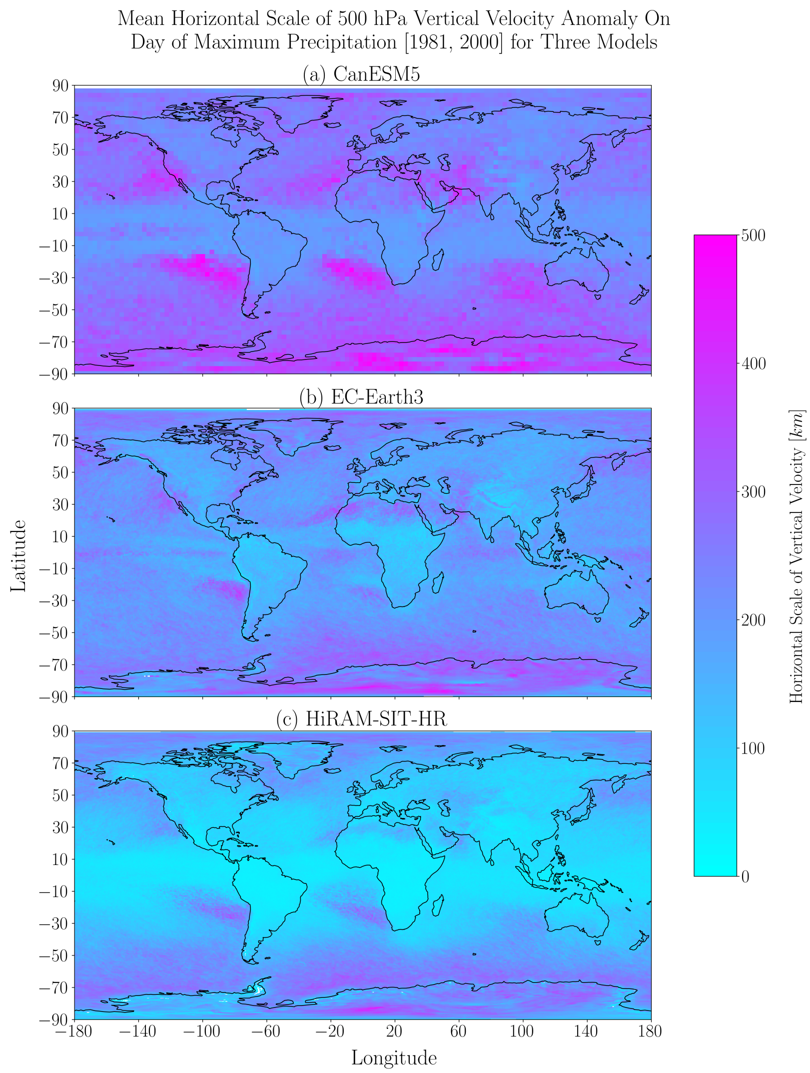

Figure 3.1: Global plots of the mean 500 hPa vertical velocity anomaly length scales for extreme precipitation events (annual maximum precipitation) from 1981 to 2000 for the (a) CanESM5, (b) EC-Earth3, and (c) HiRAM-SIT-HR models.

that at the poles. This phenomena emphasizes that length scales do not correspond directly with intensity. Many models also show a pair of minima around a local peak near the equator. This spatial structure of local minima around a local peak at the equator is also seen in the zonal mean extreme precipitation shown in figure 1 of O'Gorman and Schneider (2009a). Furthermore, there is a clear spread among the models' magnitudes for the vertical velocity length scales which again motivates further investigation into the differences between the models. For example, the local peaks near the equator for the CanESM5, EC-Earth3, and HiRAM-SIT-HR models are around 212 km, 195 km, and 64 km, respectively. The models also appear to show the most spread for values near the equator and less spread near the South Pole. For example, near 70°S the models have a spread of approximately 165 km (ranging from around 160 km to 325 km), and near 70°N the models have a similar spread of around 160 km (ranging from around 100 km to 260 km). In contrast, near the equator the models have a much larger spread of about 300 km (ranging from around 40 km to 340 km).

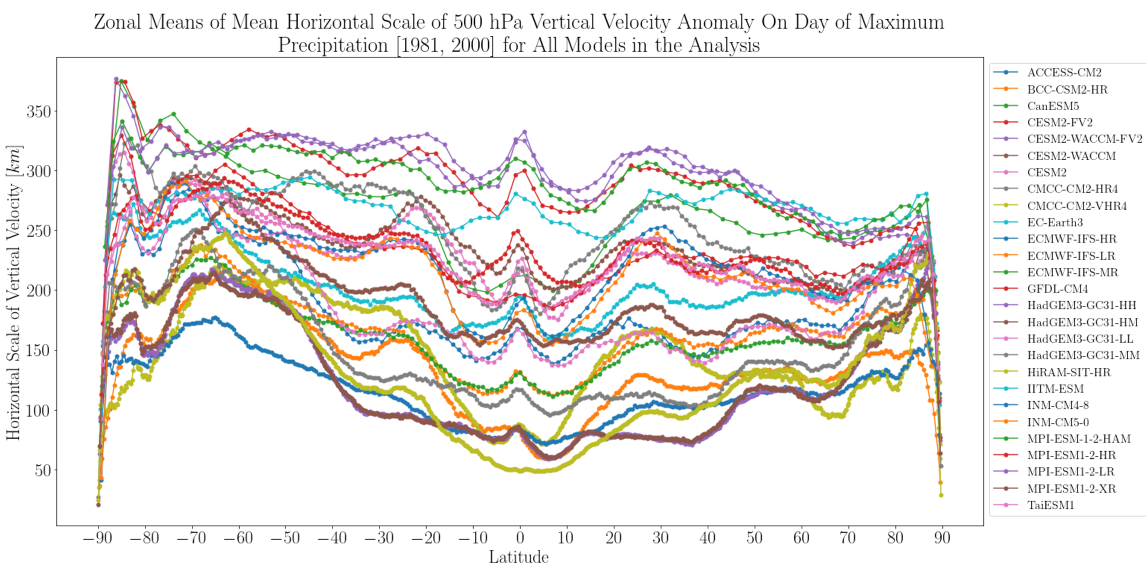

Figure 3.2: Zonal mean 500 hPa vertical velocity anomaly length scales for extreme precipitation events (annual maximum precipitation) from 1981 to 2000 for all models in the analysis.

As the global plots and zonal means of the vertical velocity length scales imply differences between the models, figure 3.3 explicitly compares the mean length scales for each model with its horizontal resolution. Indeed, figure 3.3 is the critical plot of the analysis. Figure 3.3 includes a secondary x-axis showing resolution in kilometers for grid boxes around the 55°S latitude circle. This resolution is different from the nominal resolution in table 2.2, as the grid box size varies with latitude, and the nominal resolution represents an approximate global average size of a grid box. Figure 3.3 shows a clear relationship between the mean vertical velocity length scales and the model resolution: although there is substantial scatter, the resolution appears to place an upper limit upon the length scales' magnitude that decreases as model resolution increases. The scatter between the models can be attributed to the differences between the models beyond their resolutions, such as their parameterization methods and their physics packages. Thus, though figure 3.3 shows a clear relationship influence of model resolution on extreme ascent length scales, model resolution is not the only influence. This model resolution effect is more apparent when comparing results for models that are nearly identical except for horizontal resolution. For example, the CESM2 model has a nominal resolution of 100 km and a mean length scale around 122 km, while the CESM2-FV2 model has a nominal resolution of 250 km (Zhu et al., 2022) and a mean length scale around 160 km. Similarly, the MPI-ESM1-2-HR model has a nominal resolution of 100 km and a mean length scale around 131 km, while the MPI-ESM1-2-LR model has a nominal resolution of 250 km (Gutjahr et al., 2019) and a mean length scale around 164 km. Several variants of models with the same resolution also have very similar mean length scales such as CESM2-FV2 and CESM2-WACCM-FV2 which both have length scales around 300 km, ECMWF-IFS-LR and ECMWF-IFS-MR which have length scales around 180 km, and HadGEM3-GC31-HH and HadGEM3-GC31-HM which both have length scales around 175 km. The mean length scale is also much larger than the longitudinal size of a grid box for most models.

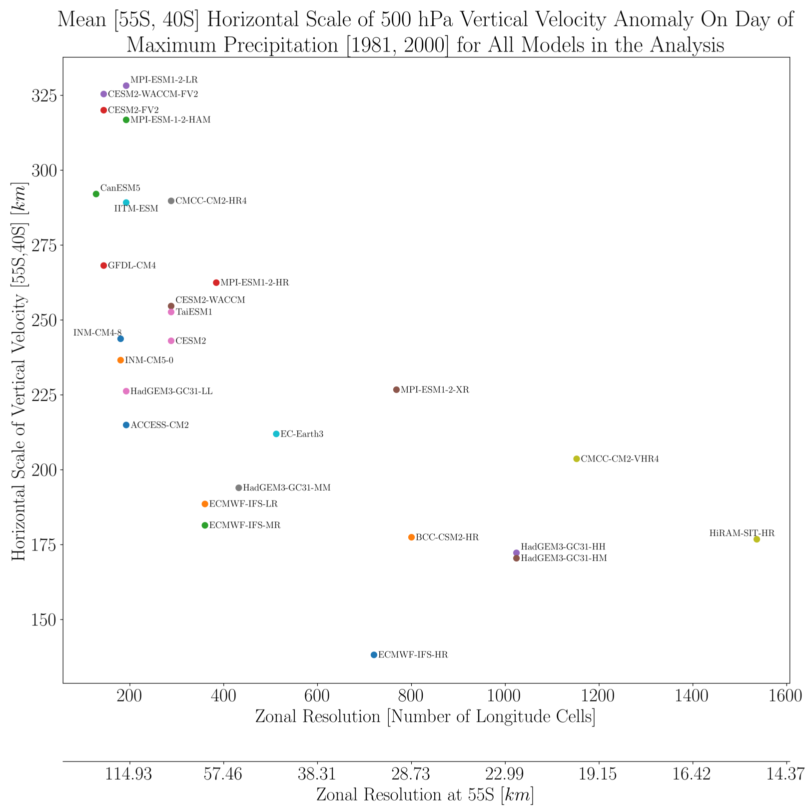

Figure 3.3: Scatter plot of the mean 500 hPa vertical velocity anomaly length scales in the 55°S to 40°S latitude range for extreme precipitation events (annual maximum precipitation) from 1981 to 2000 versus the models' zonal resolution for all models in the analysis. The secondary x-axis shows resolution in km for grid boxes around the 55°S latitude circle.

3.2 Horizontal Scales of Extreme Precipitation

As vertical velocity is a key driver of extreme precipitation, precipitation length scales are expected to follow similar behaviour as vertical velocity length scales (O'Gorman & Schneider, 2009b; Tandon, Zhang, & Sobel, 2018). So, is the model resolution effect also apparent in the precipitation length scale? Firstly, figures 3.4a, b, and c are global plots for the CanESM5, EC-Earth3 and HiRAM-SIT-HR models, respectively. The computed precipitation length scales correspond well with previous work in Dwyer and O'Gorman (2017), as they are of similar order of magnitude and have a similar spatial structure. Moreover, both studies found that though individual models have quantitative differences, they all have qualitatively similar spatial structure. However, there are some differences between the studies including the length scale computation method as Dwyer and O'Gorman (2017) exclusively use the distance east and west of an event to compute a zonal length scale, while this analysis considers distances in all four cardinal directions away from an event. Dwyer and O'Gorman (2017) also determined their length scales by using precipitation thresholds, while this study used an e-folding distance based approach. Moreover, Dwyer and O'Gorman (2017) focused on winter averages and used model output at 3-hourly and hourly temporal resolution, rather than analysing the full year at daily resolution.

The precipitation length scales follows some of the spatial behaviour that is typical for precipitation intensity, while contrasting with precipitation intensity patterns in other ways. For example, the precipitation length scales reach local maxima over oceans and around coasts and local minima within continents, however, the precipitation length scales also have local maxima in the subtropical dry zones, where precipitation is weak. Both of these behaviours were also observed for the vertical velocity length scales as seen in figures 3.1a, b, and c. The spatial structures of the two quantities are also remarkably similar, with greater magnitudes of vertical velocity length scales corresponding with those of precipitation. Moreover, though the vertical velocity and precipitation length scales are of a similar order of magnitude, the precipitation length scales are appreciably lower. For example, the global mean precipitation length scales for the CanESM5, EC-Earth3, and HiRAM-SIT-HR models are around 182 km, 171 km, and 106 km, respectively. This contrast may be due to the fact that precipitation does not vary linearly with vertical velocity at one level, and it instead relates the vertical integral of the vertical moisture transport, as discussed in section 1.7. Similar to the vertical velocity length scales, the magnitudes of precipitation length scales differ between the models, which again motivates investigation into intermodel differences.

As with the models' vertical velocity length scales, the precipitation length scales' zonal averages can be considered. Figure 3.5 shows a latitude dependence of the models with local maxima near the poles and the equator, like those in figure 3.2 for the vertical velocity length scales. Some models also show a pair of minima around a local peak near the equator, which is also seen in figure 3.2. This spatial structure of

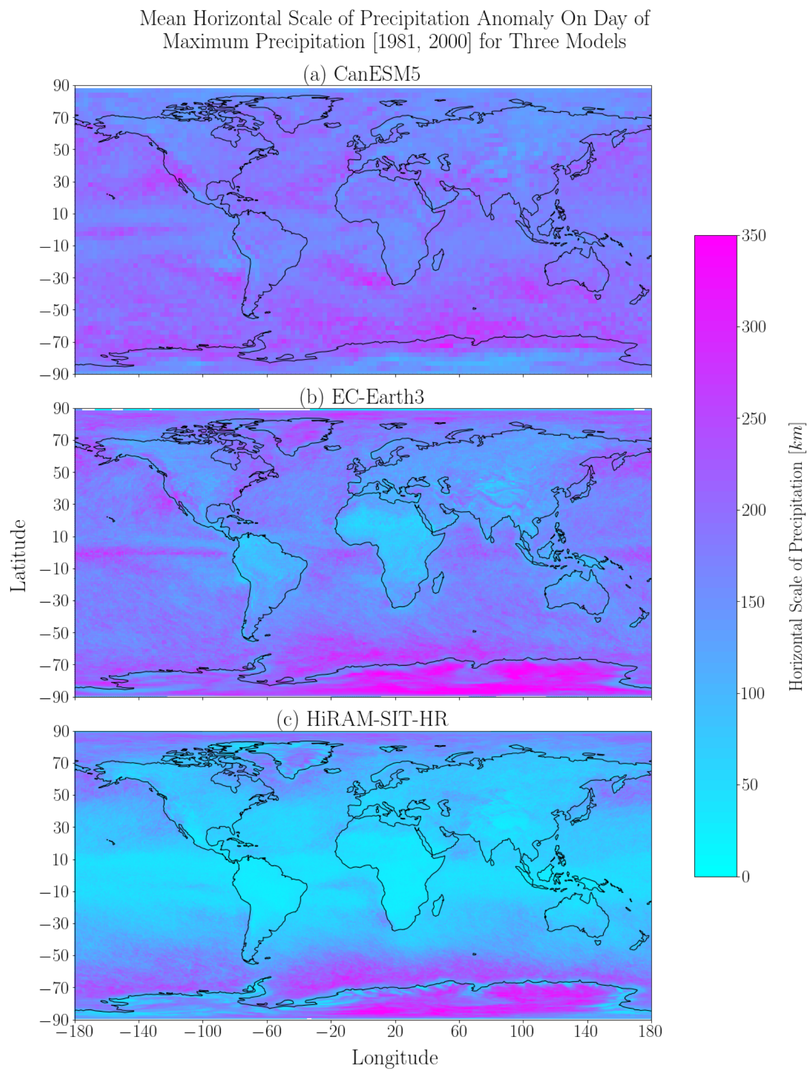

Figure 3.4: Global plots of the mean precipitation anomaly length scales for extreme precipitation events (annual maximum precipitation) from 1981 to 2000 for the (a) CanESM5, (b) EC-Earth3, and (c) HiRAM-SIT-HR models.

local minima around a local peak at the equator is also seen in the zonal mean extreme precipitation shown in figure 1 of O'Gorman and Schneider (2009a) and in figure 3.2. Like the vertical velocity length scale zonal means, there is a clear spread among the models' magnitudes for the precipitation length scales with more spread for values near the equator and less spread poleward. Clearly, like the correspondence and similarity between the the global plots for vertical velocity and precipitation length scales, there is also correspondence between the two quantities' zonal means.

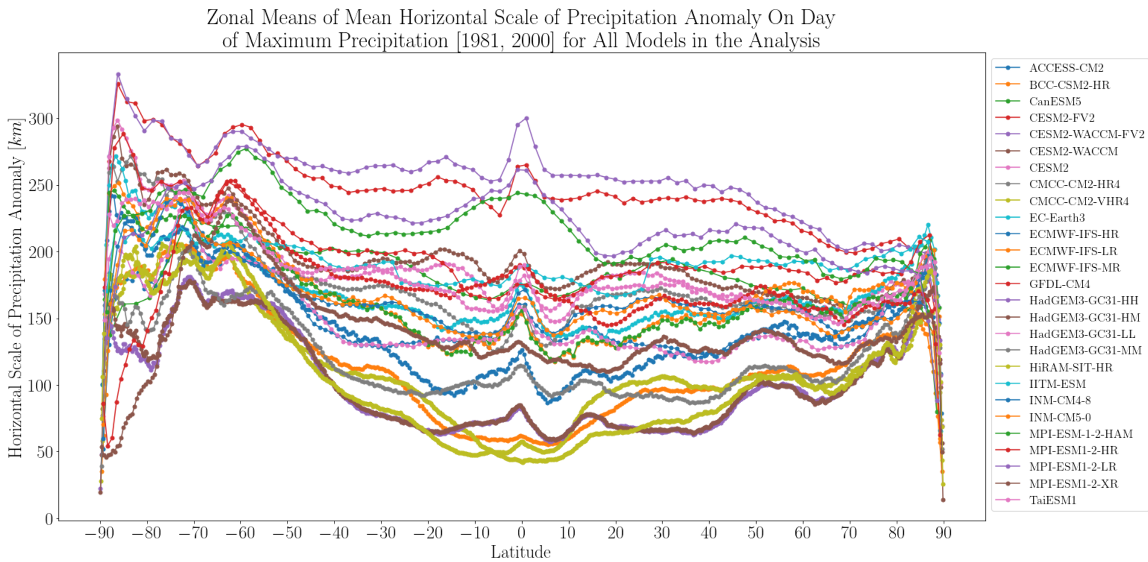

Figure 3.5: Zonal mean precipitation anomaly length scales for extreme precipitation events (annual maximum precipitation) from 1981 to 2000 for all models in the analysis.

Like the vertical velocity length scale plots, the precipitation length scale global and zonal mean plots imply differences between the models, and figure 3.6 explicitly compares the mean precipitation length scales of the models versus their zonal resolution. A similar model resolution effect as observed in the vertical velocity length scales can be observed in figure 3.6 with the model resolution appearing to place an upper limit upon the magnitude of the length scales that decreases as the resolution increases. Like the vertical velocity length scales in figure 3.3, the precipitation length scales in figure 3.6 also show scatter that can be attributed to model differences beyond model resolution, such as parameterization methods and physics packages. Similar to the vertical velocity length scales, the model resolution effect is more apparent when models that are nearly identical except for resolution are compared. For example, the CESM2 model has a nominal resolution of 100 km and a mean length scale around 187 km, while the CESM2-FV2 model has a nominal resolution of 250 km and a mean length scale around 262 km. Similarly, the MPI-ESM1-2-HR model has a nominal resolution of 100 km and a mean length scale around 200 km, while the MPI-ESM1-2-LR model has a nominal resolution of 250 km and a mean length scale around 247 km. Moreover, when compared to figure 3.3, figure 3.6 shows that the mean precipitation length scales are indeed of a similar order of magnitude as the vertical velocity length scales though appreciably lower. Like with the vertical velocity length scales, several variants of models with the same resolution also have very similar mean length scales such as INM-CM5-0 and INM-CM4-8 which have length scales around 170 km, ECMWF-IFS-LR and ECMWF-IFS-MR which have length scales around 185 km, and HadGEM3-GC31-HH and HadGEM3-GC31-HM which have length scales around 135 km.

How do the model results for the precipitation length scales compare with observational results? Figure 3.6 includes the mean precipitation length scales computed from three observational data sets, CMORPH, IMERG, and GPCP V3.2 from 2001 to 2014. The mean length scales for CMORPH and IMERG are very similar at around 143 km. As mentioned in the methods section, CMORPH incorporates GPCP V3.2, and GPCP V3.2 incorporates IMERG, but CMORPH and IMERG's mean length

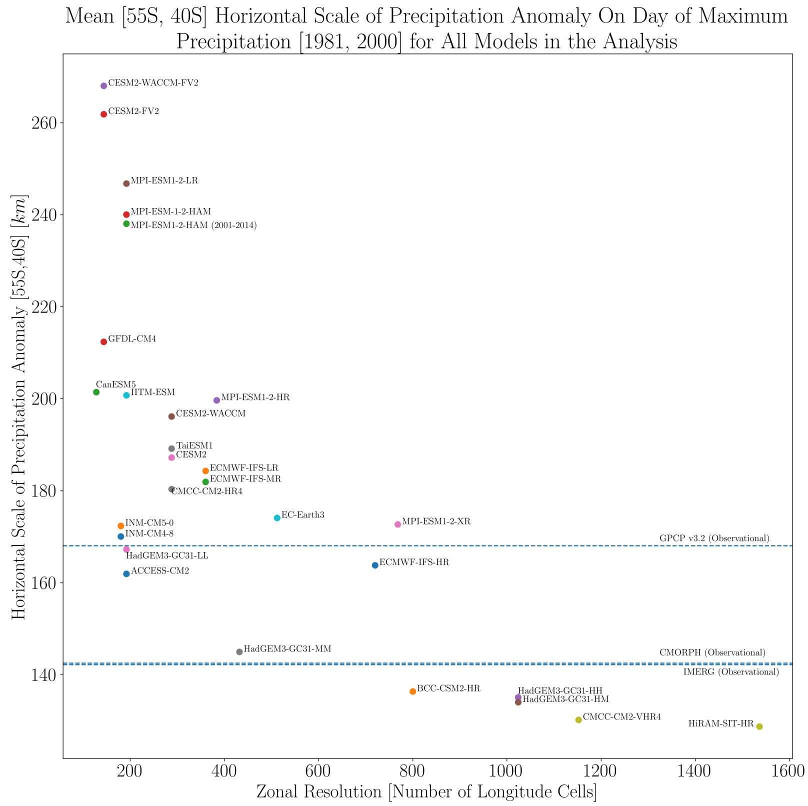

Figure 3.6: Scatter plot of the precipitation anomaly length scales in the 55°S to 40°S latitude range for extreme precipitation events (annual maximum precipitation) from 1981 to 2000 versus the models' zonal resolution for all models in the analysis, including observational results from CMORPH, IMERG, and GPCP V3.2 from 2001 to 2014, and an additional result for the MPI-ESM-1-2-HAM model, also computed from 2001 to 2014.

scales are much closer to each other than they are to GPCP V3.2's mean length scale of around 168 km. However, due to differences in algorithms and measurement instruments perfect agreement between different observational datasets is not expected.

The ACCESS-CM2, HadGEM3-GC31-LL, HadGEM3-GC31-MM, and ECMWF-IFS-HR models fall within the range produced by the observational results, with nominal resolutions of 250 km, 250 km, 100 km, and 25 km respectively. Though there is no clear relationship between model resolution and agreement with observational results, intriguingly, the highest resolution models do not appear to produce results closest to the observational results. To assess possible sensitivity to the choice of time period, Figure 3.6 also includes a second point for the MPI-ESM-1-2-HAM model, corresponding to model results from 2001 to 2014. By comparing the MPI-ESM-1-2-HAM model's results from 1981 to 2000 to those from 2001 to 2014, it is clear that time period has little influence on the horizontal scale. Thus, model results computed from 1981 to 2000 can be compared with the observational results computed from 2001 to 2014. Similar to checking possible sensitivities to choice of time period, additional analysis checked possible sensitivity to choice of ensemble member. Modelling centres often run models under many slightly different initial conditions, each one referred to as an ensemble member, to produce a spread of model output to account for the sensitivity of the model to initial conditions (eg., Deser et al., 2010). Thus, it is important to confirm that the length scales computed from the models are not affected by the noise different initial conditions introduce, these ensemble members have slightly different internal climates that may effect length scales. However, length scales computed from alternate realizations of the MPI-ESM1-2-HAM model confirmed that the spatial scales are not sensitive to internal climate variability as means computed from different ensemble members differed negligibly (not shown).

3.3 Horizontal Scales of Grid Scale and Parameterized Precipitation

In CMIP6 models (and many climate models in general), total precipitation is summed from two components. The first component is precipitation that is resolved at the grid scale, while the second component is from parameterization that aims to capture convection that occurs at the sub-grid scale. In the modelling community, both forms of precipitation are referred to with various terminology, which can create confusion. For example, in CMIP6 archives and documentation, the latter is referred to as "convective precipitation," even though it does not include precipitation due to grid-scale convection, which is an important consideration in this analysis. Moreover, "convective precipitation" is sometimes also referred to as "cumulus precipitation" even though not all parameterized precipitation is due to cumulus convection. Similarly, precipitation resolved at the grid scale is often referred to as "large scale" or "stratiform" precipitation even though "large-scale" is vague and not all precipitation resolved at the grid scale is stratiform. To avoid confusion, the two forms of precipitation are referred to hereafter as "grid-scale precipitation" and "parameterized precipitation".

What is the relative contribution of each component of precipitation on the behaviour of the total precipitation spatial scale? Figure 3.7a is a scatter plot of the mean length scales of grid scale precipitation, which clearly shows that the grid scale precipitation length scales follow a similar model resolution effect as the length scales for vertical velocity and total precipitation: the model resolution appears to place an upper limit upon the length scales that decreases as resolution increases. Similar to the vertical velocity and precipitation length scales, the model resolution effect is more apparent when models that are nearly identical except for resolution are compared. For example, the CESM2 model has a nominal resolution of 100 km and a mean length scale around 187 km, while the CESM2-FV2 model has a nominal resolution of 250 km and a mean length scale around 258 km (Zhu et al., 2022). Similarly, the MPI-ESM1-2-HR model has a nominal resolution of 100 km and a mean length scale around 200 km, while the MPI-ESM1-2-LR model has a nominal resolution of 250 km and a mean length scale around 247 km (Gutjahr et al., 2019). Moreover, similar to the vertical velocity and precipitation length scales, several variants of models with the same resolution also have very similar mean length scales such as INM-CM5-0 and INM-CM4-8 which have length scales around 170 km, ECMWF-IFS-LR and ECMWF-IFS-MR which have length scales around 180 km, and HadGEM3-GC31-HH and HadGEM3-GC31-HM which have length scales around 148 km. The grid scale precipitation length scales for all pairs of models mentioned here are also very similar to their total precipitation length scales. Figure 3.7c is a scatter plot of the mean total precipitation length scales versus the mean grid scale level precipitation length scales and shows that the two quantities have very similar magnitudes, falling very close to the one-to-one line. Some models in figure 3.7c appear to have slightly greater grid scale precipitation length scales than total precipitation length scales such as IITM-ESM which had a total precipitation length scale around 201 km and a grid scale precipitation length scale around 211 km, and MPI-ESM1-2-HAM which had a total precipitation length scale around 240 km but a grid scale precipitation length scale around 250 km. This is not so surprising, since as discussed earlier, precipitation spatial scale and precipitation intensity do not have a straightforward relationship. Figure 3.7d shows that grid scale precipitation anomaly intensity is roughly proportional to total precipitation anomaly intensity for most models, though some models show no clear proportionality between the two quantities. Regardless of proportionality, figure 3.7d also shows that grid scale precipitation anomalies account for at least 50% of the precipitation anomalies for all models, over 75% for most models, and close to 100% for many models. It also appears that for the models with the highest extreme precipitation intensities (precipitation anomaly over 25 mm day^{-1}) almost all of their precipitation is due to grid scale precipitation.

Figure 3.7b is a scatter plot of the length scales for parameterized precipitation versus model resolution. Unlike the length scales for vertical velocity, total precipitation, and grid scale precipitation, figure 3.7b shows that the model resolution effect is not as clear for parameterized precipitation. However, if the outlier CMCC-CM2-HR4 model is ignored, the model resolution effect is more clear. More work is needed to determine why the sub grid scale parameterized precipitation length scales may be resolution dependent. Other than the CMCC-CM2-HR4 model the parameter-

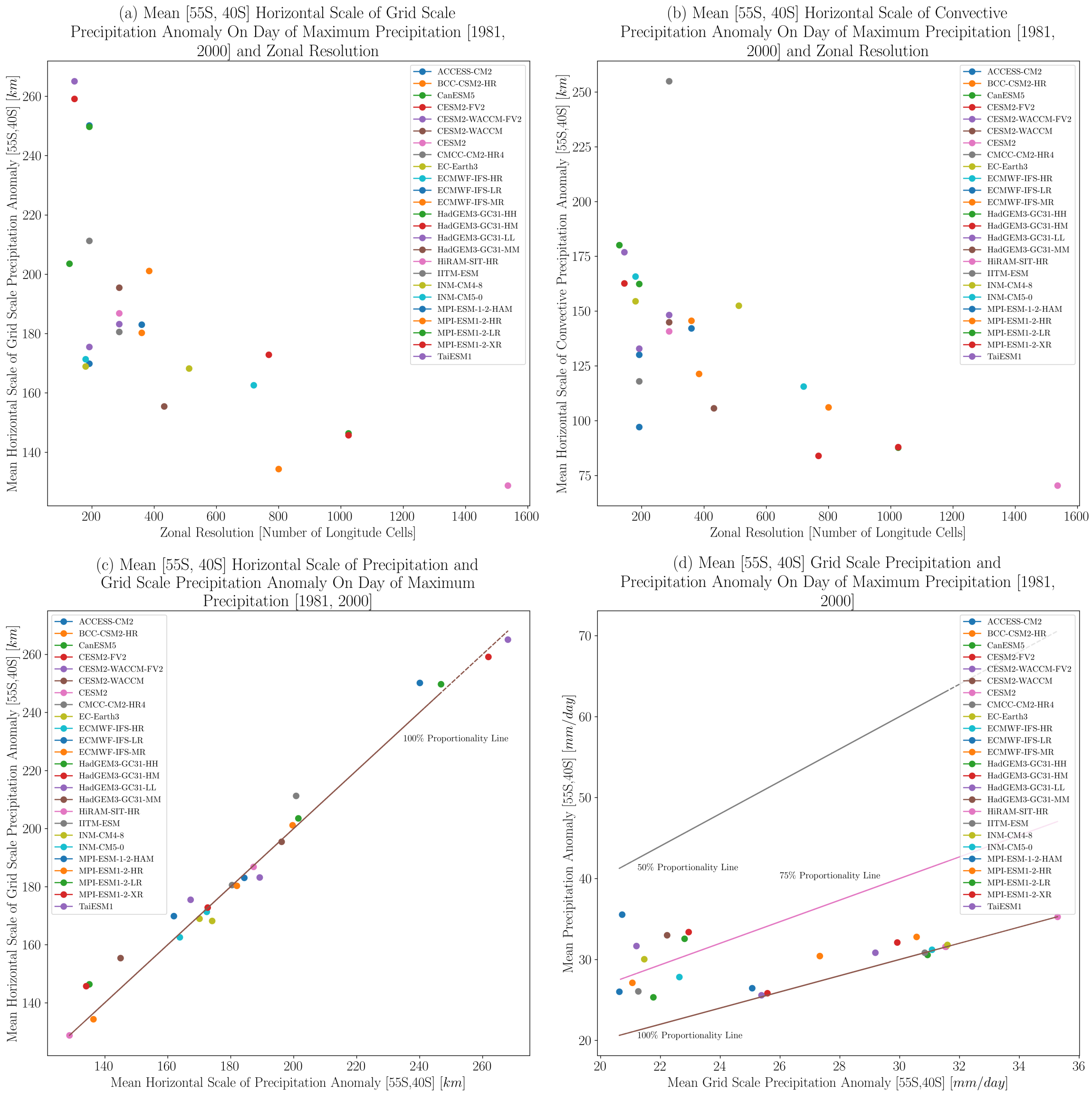

Figure 3.7: (a) The grid scale precipitation anomaly length scales versus the models' zonal resolution. (b) The parameterized precipitation anomaly length scales versus the models' zonal resolution. (c) The precipitation anomaly length scales versus the grid scale precipitation anomaly length scales. (d) The grid scale precipitation anomaly versus the total precipitation anomaly, including lines indicating grid scale precipitation that is 100%, 75%, and 50% of the total precipitation. All quantities are averaged in the 55°S to 40°S latitude range for extreme precipitation events (annual maximum precipitation) from 1981 to 2000.

ized precipitation length scales range from around 60 km to 180 km while the grid scale precipitation length scales range from around 125 km to 270 km. Clearly, for most models the parameterized precipitation length scales are of lower magnitude than the grid scale precipitation length scales, and they do not account for the total precipitation length scales.

3.4 Role of Large-Scale Dynamics

The apparent greater contribution of the grid scale precipitation length scales than the parameterized precipitation length scales to the total precipitation length scales can be due to two possibilities. Firstly, the models' large scale dynamics, which contribute significantly to precipitation events in the midlatitudes and extratropics, may be resolution dependent. As grid scale precipitation can be associated with large scale dynamics in models, a resolution-dependence of the large scale dynamics might explain the resolution-dependence in extreme ascent and grid-scale precipitation. Secondly, the models may not be producing enough parameterized precipitation due to convecting at the grid scale rather than the sub grid scale, decreasing the intensity of parameterized precipitation and increasing the intensity of grid scale precipitation. In the midlatitudes and extratropics, variations in the geopotential correspond to those large scale dynamics, therefore the length scales of geopotential can be investigated to gauge the influence of the models' large scale dynamics on their precipitation length scales.

Figures 3.8a, b, and c are typical global plots of geopotential length scales for the CanESM5, EC-Earth3, and HiRAM-SIT-HR models, respectively. The geopotential length scales reach a maximum around the equator and decrease elsewhere, which is unlike the behaviour seen in the vertical velocity and precipitation length scales. Moreover, comparing the zonal means of the vertical velocity, precipitation, and geopotential length scales (figures 3.2, 3.5, and 3.9, respectively) shows that the geopotential length scales decrease roughly monotonically away from the equator with much less pronounced local maxima in the midlatitudes than the vertical velocity and precipitation length scale. Moreover, though the length scale for vertical velocity, precipitation, and geopotential all show peaks near the equator, this is a global peak for the geopotential length scales, and a local peak for vertical velocity and precipitation (their global peaks tend to be near the poles). Like the vertical velocity length scales, the precipitation and geopotential length scales show more spread for values near the equator and less spread poleward, except for right at the poles. The geopotential length scale magnitudes are remarkably similar outside of the tropics. While the vertical velocity and precipitation length scales are of a similar order of magnitude, the geopotential length scales are much greater. For example, the global mean geopotential length scales for the CanESM5, EC-Earth3, and HiRAM-SIT-HR models are around 880 km, 900 km, and 798 km, respectively. Interestingly, the HiRAM-SIT-HR model has a peak slightly south of the equator, though more work is needed to determine why this is the case.

The geopotential length scale results can also be investigated with respect to their model resolution, as shown in figure 3.10. Unlike the length scales for vertical velocity, total precipitation, and grid scale level precipitation, the geopotential length scales show no clear model resolution influence and thus the large scale dynamics of the models show no clear resolution dependence, eliminating this as a potential explanation for the apparent significance of grid scale precipitation on extreme precipitation in the the models. While the results have shown some correspondence between the vertical velocity, precipitation, and grid scale precipitation length scales, there is no clear correspondence between the geopotential length scales and precipitation or grid scale precipitation. Moreover, additional model analysis (not shown) has revealed that the timing of extreme precipitation events coincides with peaks in vertical instability, as is expected from basic theory, so convection at some scale is indeed associated with extreme precipitation events. Both the correspondence between precipitation and grid scale precipitation and the vertical instability timing phenomenon can be explained by the models convecting at the grid scale rather than the sub-grid scale. If the models were convecting primarily at the sub-grid scale, one may expect parameterized precipitation to account for most of the total precipitation intensity or length scale, which is not the case. All these findings together raise the possibility that the apparent greater contribution of the grid scale precipitation length scales than the parameterized precipitation length scales to the total precipitation length scales can be explained by the models convecting at the grid scale. Another possibility worth exploring in future studies could be the role of baroclinic instability associated with strong localised fronts that could be driving the extreme ascent.

However, this dominance of grid scale precipitation in the models is not realistic as convective precipitation is expected to contribute strongly to extreme precipitation events (Berg, Moseley, & Haerter, 2013; Park & Min, 2017; Roca & Fiolleau, 2020). Notably, models that show the lowest percentage of grid scale precipitation to total precipitation are also among the models that are closest to the horizontal scales of precipitation based on observational data. For example, the ACCESS-CM2, HadGEM3-GC31-LL, HadGEM3-GC31-MM, and ECMWF-IFS-HR models had percentages of 58.3%, 67.0%, 67.4%, and 81.3%, respectively, which correspond to the lowest, second lowest, third lowest, and ninth lowest percentages of 25 models and all four models produced precipitation length scales that fell within the range produced by the observational data sets. A lower proportion of grid scale precipitation means a higher proportion of parameterized precipitation, so these results suggest that model improvements that increase the proportion of parameterized precipitation during extreme precipitation events may be successful in improving the representation of extreme precipitation spatial scales. Though there are some models with high proportions of grid scale precipitation that also happen to produce precipitation spatial scales close to the observed range, there is little consistency as most of the models with high proportions of grid scale precipitation did not produce spatial scales close to observations, whereas all of the models with lower proportions of grid scale precipitation produce spatial scales close to observations.

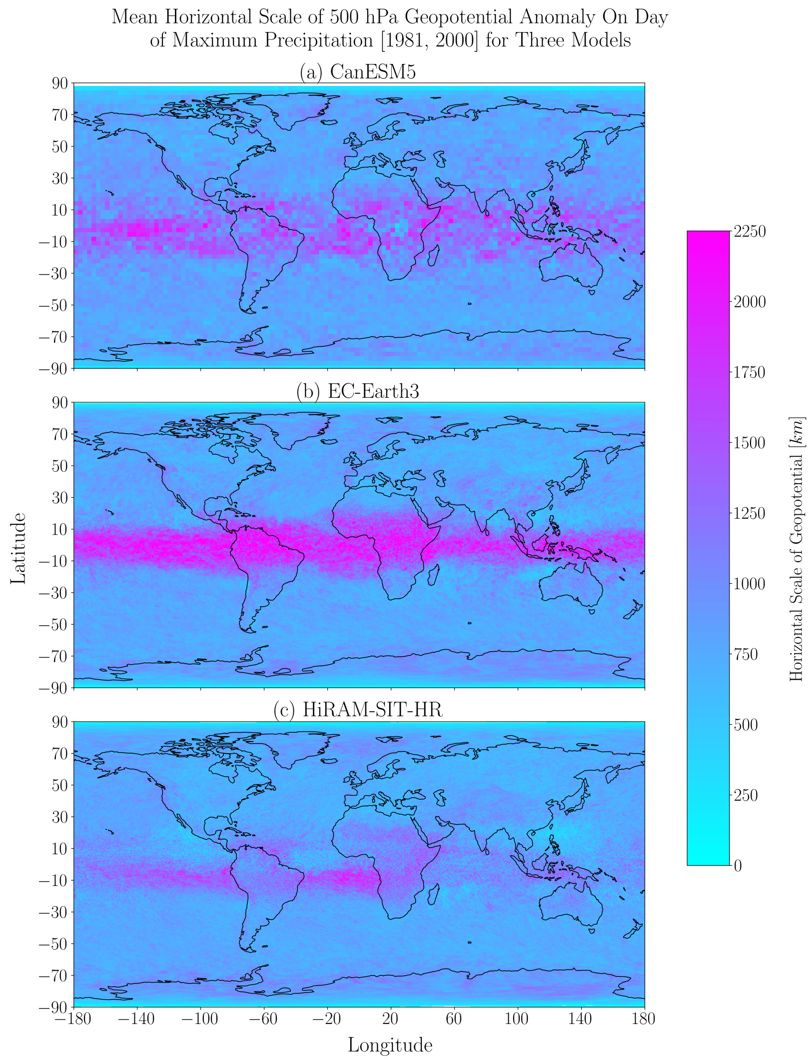

Figure 3.8: Global plots of the mean 500 hPa geopotential anomaly length scales for extreme precipitation events (annual maximum precipitation) from 1981 to 2000 for the (a) CanESM5, (b) EC-Earth3, and (c) HiRAM-SIT-HR models.

In comparison to previous work in Kidston et al. (2010), the computed geopotential length scales are of similar order of magnitude (note the 2π factor difference between the length scales shown by Kidston et al. (2010), as they show wavelengths instead of the inverse wavenumbers shown here). However, only a minority of models

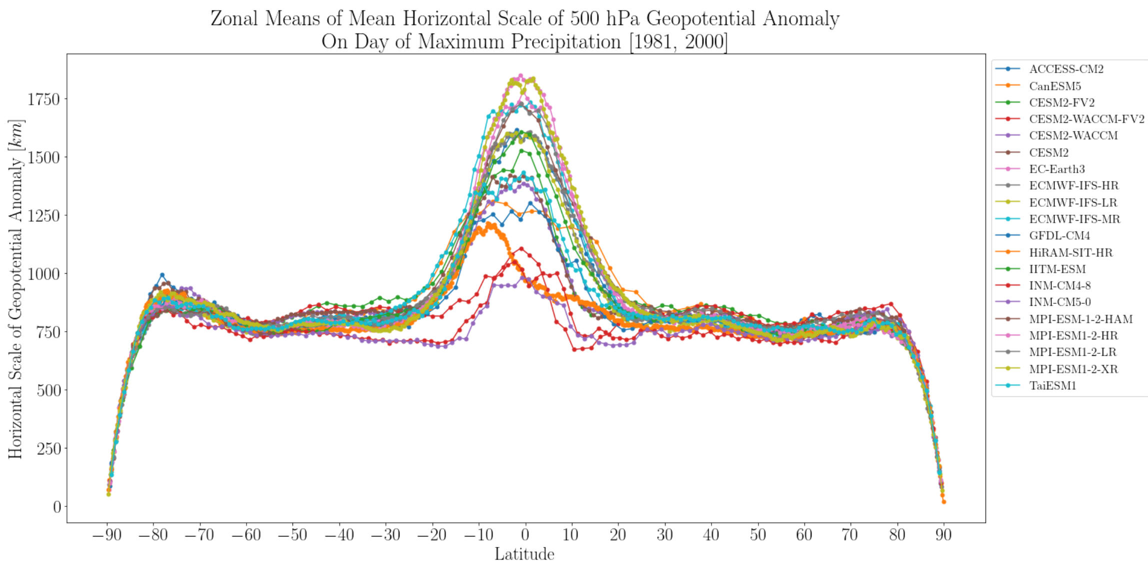

Figure 3.9: Zonal mean 500 hPa geopotential anomaly length scales for extreme precipitation events (annual maximum precipitation) from 1981 to 2000.

in Kidston et al. (2010) showed similar zonal structure to the models shown here, with their length scales peaking close to the equator and decreasing with latitude away from the equator. Full agreement between the studies is not expected as they have appreciable differences, including in methodology, as Kidston et al. (2010) decomposed meridional wind speed at 300 hPa into Fourier components around latitude circles to compute eddy length scales for events over the entire 1981 to 2000 epoch. In contrast, this analysis used an e-folding approach in four cardinal directions to compute length scales from geopotential at 500 hPa for annual maximum precipitation events. Moreover, this analysis used model output from CMIP6 while Kidston et al. (2010) used model output from CMIP3.

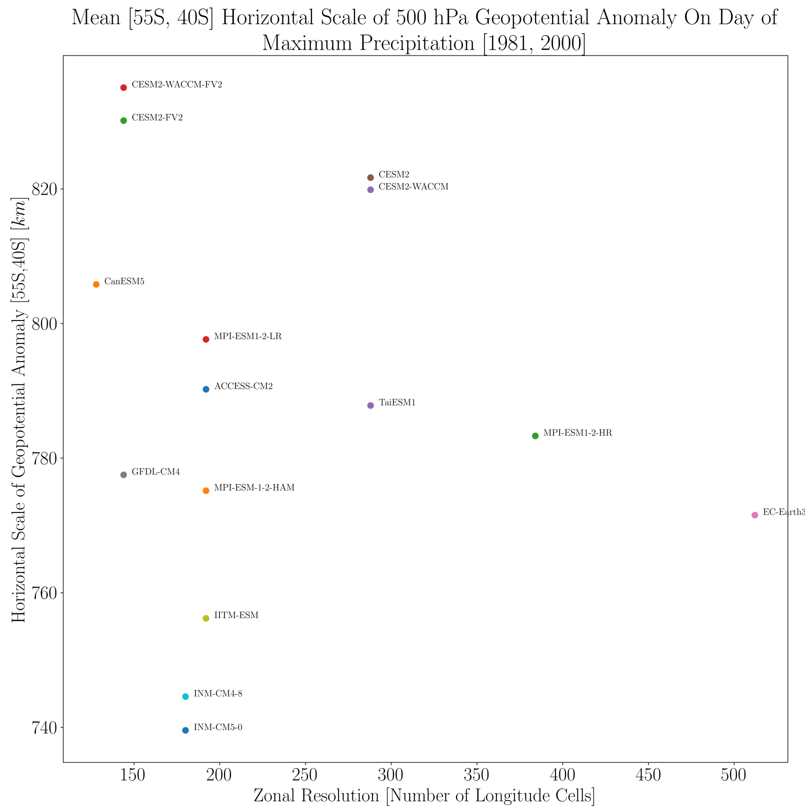

Figure 3.10: Scatter plot of the mean 500 hPa geopotential anomaly length scales in the 55°S to 40°S latitude range for extreme precipitation events (annual maximum precipitation) from 1981 to 2000 versus the models' zonal resolution.

3.5 Sensitivity Tests

As this analysis relies on computed horizontal scales from models for EPEs, it is important to confirm that the results are not simply a product of grid box storms. If extreme precipitation events in the models were grid box storms, the computed length scales would simply correspond with the size of the grid box leading to a proportional relationship between model resolutions and length scales. Figure 3.11 is a scatter plot of the annual mean percentage of vertical velocity length scales that are larger than a grid box in each dimension. For all models, the overwhelming majority of length scales are indeed larger than a grid box in both dimensions, confirming that the resolution dependence of the extreme precipitation events realized in the models cannot be simply explained by grid box storms. Models in figure 3.11 range from 76% (for CMCC-CM2-VHR4) to 98% (for IITM-ESM1). There is also a rough proportionality between the percentage of length scales larger than a grid box in each dimension, indicating that the storms are not simply stretched zonally and accounting for the length scales in all four cardinal directions can be a correct approach to determining the spatial scales of the EPEs. The largest differences between percentages in each direction are for the ACCESS-CM2 and HadGEM3-GC31-LL models, which were both 5% greater for horizontal scales larger than a latitude band than those for a longitude band. ACCESS-CM2 and HadGEM3-GC31-LL were also only two of six models (the other four are GFDL-CM4, HadGEM3-GC31-HH, HadGEM3-GC31-HM, HadGEM3-GC31-MM) that showed larger percentages for horizontal scales larger than a latitude band than for a longitude band; all other models either had equal percentages, or greater percentages for horizontal scales larger than a longitude band.

Additional analysis (not shown) has confirmed that the length scales are not sensitive to the choice of time resolution, so a daily temporal resolution can be used to correctly identify and study EPEs in the models. One may expect longer time scales to lead to larger length scales, as the storm can move around leading to higher values of extreme ascent or precipitation in neighbouring locations, and shorter time

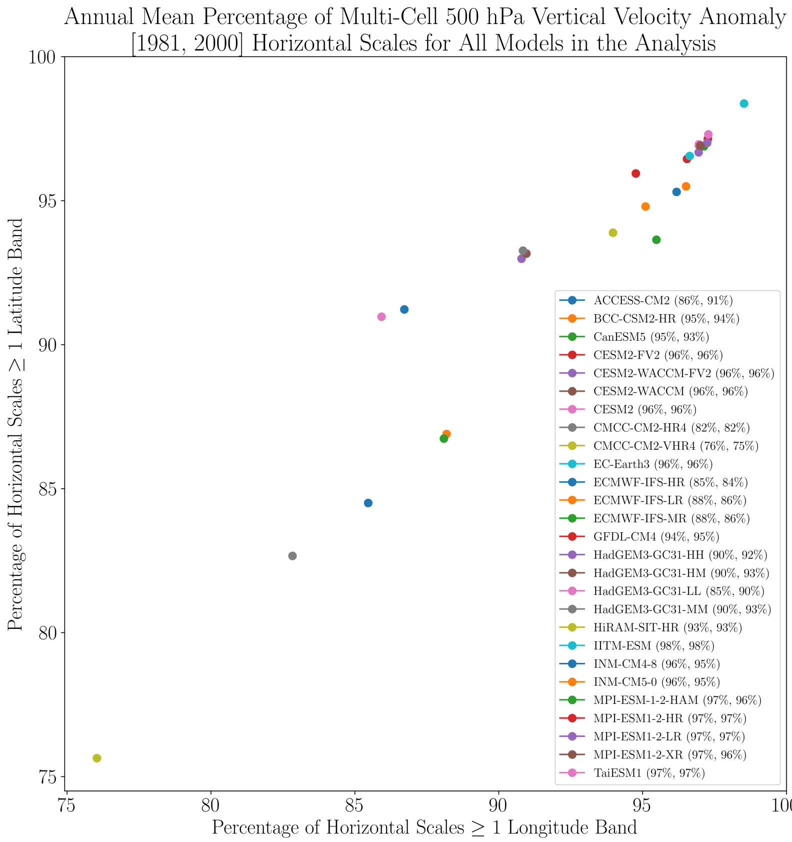

Figure 3.11: Scatter plot of the annual mean percentage of 500 hPa length scales that are greater than a longitude band versus the percentage greater than a latitude band, for all models in the analysis. The legend indicates the scatter plot point color, model name, and the coordinates of the point.

scales to lead to shorter length scales due to the storm moving less. However, analysis of the MPI-ESM1-2-HAM model showed that this effect was not significant when comparing results from three-hourly accumulated precipitation to seven-day accumulated precipitation. Finally, as mentioned earlier, additional analysis of alternate realizations of the MPI-ESM1-2-HAM model confirmed that the spatial scales are not sensitive to internal climate variability, as means computed from different ensemble members differed negligibly.

4 Conclusion

Our results show that the vertical velocity length scales for extreme precipitation events in climate models have qualitatively similar zonal structure including peaks at the poles and local peaks near the equator and generally greater magnitudes over the ocean than over land. However, the models did not show any simple correspondence between extreme ascent strength and extreme ascent length scales, as has been noted in previous studies such as (Tandon, Zhang, & Sobel, 2018). The average magnitude of the length scales also clearly differed between the models motivating further investigation into the differences between the models. An explicit comparison between the mean length scales for each model with its horizontal resolution has revealed that the resolution appears to place an upper limit upon the length scales' magnitude that decreases as model resolution increases. Though the model resolution effect is clear, there is scatter among the models that can be attributed to differences between the models beyond their model resolutions, such as parameterization methods and physics packages.

This model resolution effect for vertical velocity length scales motivated analysis of precipitation length scales as the two are expected to follow similar behaviour. In comparison with the vertical velocity length scales, the precipitation length scales have similar spatial structure and order of magnitude though the precipitation length scales are appreciably lower. The precipitation length scales results also show the model resolution effect as the model resolution appears to place an upper limit upon the magnitude of the length scales that decreases as the resolution increases. The computed precipitation length scales also correspond well with previous work in Dwyer and O'Gorman (2017), as they are of similar order of magnitude and have a similar spatial structure. In comparison to precipitation length scales computed from the CMORPH, IMERG, and GPCP V3.2 observational datasets from 2001 to 2014, only four models fell within the range produced by the observational results. Moreover, the highest resolution models did not appear to produce results closest to the observational results.

Precipitation is summed from grid scale precipitation and parameterized precipitation in CMIP6 models. Investigating these individual components of precipitation revealed that the grid scale level precipitation length scales follow a similar model resolution effect as those for vertical velocity and total precipitation; the model resolution appears to place an upper limit upon the length scales that decreases as resolution increases. Moreover, a comparison of precipitation and grid scale level precipitation length scales shows that the two quantities have very similar magnitudes and are approximately proportional. The intensity of grid scale precipitation anomalies was also roughly proportional to precipitation anomaly intensity for most models, though other models showed no clear proportionality between the quantities. Regardless of proportionality, grid scale precipitation anomalies account for at least 50% of the precipitation anomalies for all models, and over 75% for most models. In contrast, parameterized precipitation did not show a clear model resolution effect and was less significant than grid scale precipitation in the models for extreme precipitation events. Moreover, models that show the lowest percentage of grid scale precipitation to total precipitation are also among the models that are closest to the horizontal scales of precipitation based on observational data. These results suggest that model improvements that increase parameterized precipitation during extreme precipitation events may be successful in improving the representation of extreme precipitation spatial scales.

The greater contribution of grid scale precipitation than parameterized precipitation length scales to extreme precipitation length scales can be due to two possibilities: a resolution dependence of the models' large scale dynamics, or, the models not producing enough convective precipitation at the sub grid scale due to convecting at the grid scale. Variations in the geopotential correspond to large scale dynamics in the midlatitudes and extratropics, thus geopotential length scales were investigated to gauge the influence of the models' large scale dynamics on their precipitation length scales. In comparison to the vertical velocity and precipitation length scales, the geopotential length scales showed much greater magnitudes, completely different spatial structure, and no clear model resolution influence. Thus, the large scale dynamics of the models showed no clear resolution dependence. While the vertical velocity, precipitation, and grid scale precipitation length scales showed correspondence, there is no clear correspondence between the geopotential length scales and those for precipitation or grid scale precipitation. Moreover, additional model analysis (not shown) revealed that the timing of extreme precipitation events coincides with peaks in vertical instability. Both the correspondence between precipitation and grid scale precipitation and the vertical instability timing phenomenon can be explained by the models convecting at the grid scale rather than the sub-grid scale. Additional model analysis (not shown) also revealed that the timing of extreme precipitation events coincides with peaks in vertical instability, so convection at some scale is indeed associated with extreme precipitation events in the models. This significance of grid scale precipitation in the models is not realistic as convective precipitation is expected to contribute strongly to extreme precipitation events (Berg, Moseley, & Haerter, 2013; Park & Min, 2017; Roca & Fiolleau, 2020). Future studies can explore the possible role of baroclinic instability associated with strong localised fronts that could be driving extreme ascent.

Though increasing model resolution is often a simple and successful approach to improving model simulations, it may not be the best approach for improving model simulations of extreme precipitation events as the realism of convection parameterization will not necessarily improve under increased resolutions. However, if model resolution can be increased to a point such that convection can be explicitly resolved (around 10 km or less) then increased resolution can potentially improve extreme precipitation event simulation. However, it is currently computationally prohibitive to run climate simulations with such global convection-resolving models. An attractive compromise can be to run convection-resolving models over a limited domain, but the boundary conditions needed for such simulations typically come from global climate models that parameterize convection, so such an approach does not guarantee greater realism.

Additional sensitivity analysis showed the length scale results are not simply a product of grid box storms as the overwhelming majority of length scales are larger than a grid box in both dimensions. Additional analysis (not shown) has confirmed that the length scales are not sensitive to the choice of time resolution. Moreover, length scales computed from alternate realizations of the MPI-ESM1-2-HAM model confirmed that the spatial scales are not sensitive to internal climate variability.

One limitation of this study was the codependence of the observational results used for comparison. Though CMORPH, IMERG, and GPCP V3.2 datasets provided suitable precipitation observations for this analysis, and they all incorporate each other somewhat as GPCP V3.2 uses IMERG as an input in the 55°N to 55°S latitude range and CMORPH uses GPCP for bias correction over the ocean. In general, more independent observational precipitation datasets are needed in order to provide a strong basis for comparison with models. While this study already includes several models that were run at varying resolutions (MPI-ESM-1-2-LR and MPI-ESM-1-2-HR or HadGEM3-GC31-LL and HadGEM3-GC31-HH, for example), as an extension to this study, an individual model can be run over a wider range of spatial resolutions in order to assess the influence of spatial resolution in more detail and explore possible solutions. Changing the model resolution for individual models is non-trivial however, as parameterization methods often need to be completely readjusted with each choice of resolution. Our analysis reveals that model improvements that increase the proportion of convective precipitation during EPEs should also improve the representation of EPE spatial scale. Thus, additional work is needed to understand what changes need to be made in models in order to make the amount of convective precipitation during EPEs more realistic. This might involve adjustments to the model's entrainment parameter, changes to the convection triggering schemes, or modifications to the adjustment process for gridbox supersaturation.

Bibliography

Barnes, E. A., & Hartmann, D. L. (2012). The Global Distribution of Atmospheric Eddy Length Scales. *Journal of Climate*, *25*. https://doi.org/10.1175/JCLI-D-11-00331.1

Berg, P., Moseley, C., & Haerter, J. O. (2013). Strong increase in convective precipitation in response to higher temperatures. *Nature Geoscience*, *6*. https://doi.org/10.1038/ngeo1731

Cam6 scientific guide [Accessed: 2023-05-05]. (2017). %5Curl%7Bhttps://ncar.github.io/CAM/doc/build/html/cam6_scientific_guide/physics.html%7B%5C#%7Ddeep-convection%7D

Chan, S. C., Kendon, E. J., Roberts, N. M., Fowler, H. J., & Blenkinsop, S. (2016). The characteristics of summer sub-hourly rainfall over the southern uk in a high-resolution convective permitting model. *Environmental Research Letters*, *11*. https://doi.org/10.1088/1748-9326/11/9/094024

Deser, C., Phillips, A., Bourdette, V., & Teng, H. (2010). Uncertainty in climate change projections: The role of internal variability. *Climate Dynamics*, *38*. https://doi.org/10.1007/s00382-010-0977-x

Dwyer, J. G., & O'Gorman, P. A. (2017). Changing duration and spatial extent of midlatitude precipitation extremes across different climates. *Geophysical Research Letters*, *44*. https://doi.org/10.1002/2017GL072855

Eyring, V., Bony, S., Meehl, G. A., Senior, C. A., Stevens, B., Stouffer, R. J., & Taylor, K. E. (2016). Overview of the coupled model intercomparison project phase 6 (cmip6) experimental design and organization. *Geoscientific Model Development*, *9*. https://doi.org/10.5194/gmd-9-1937-2016

Gutjahr, O., Putrasahan, D., Lohmann, K., Jungclaus, J. H., von Storch, J.-S., Brüggemann, N., Haak, H., & Stössel, A. (2019). Max planck institute earth system model (mpi-esm1.2) for the high-resolution model intercomparison project (highresmip). *Geoscientific Model Development*, *12*. https://doi.org/10.5194/gmd-12-3241-2019

Haarsma, R. J., Roberts, M. J., Vidale, P. L., Senior, C. A., Bellucci, A., Bao, Q., Chang, P., Corti, S., Fučkar, N. S., Guemas, V., von Hardenberg, J., Hazeleger, W., Kodama, C., Koenigk, T., Leung, L. R., Lu, J., Luo, J.-J., Mao, J., Mizielinski, M. S., … von Storch, J.-S. (2016). High resolution model intercomparison project (highresmip v1.0) for cmip6. *Geoscientific Model Development*, *9*. https://doi.org/10.5194/gmd-9-4185-2016

Hartmann, D. L. (2016). *Global physical climatology*. Elsevier Inc.

Huffman, G., Behrangi, A., Bolvin, D., & Nelkin, E. (2022). GPCP Version 3.2 Daily Precipitation Data Set, Edited by G.J. Huffman, A. Behrangi, D.T. Bolvin, E.J. Nelkin. *Goddard Earth Sciences Data and Information Services Center (GES DISC)*. https://doi.org/10.5067/MEASURES/GPCP/DATA305

Huffman, G., Stocker, E., Bolvin, D., Nelkin, E., & Tan, J. (2019). GPM IMERG Final Precipitation L3 1 day 0.1 degree x 0.1 degree V06, Edited by Andrey Savtchenko. *Goddard Earth Sciences Data and Information Services Center (GES DISC)*. https://doi.org/10.5067/GPM/IMERGDF/DAY/06

Idf curve [Accessed: 2023-05-05]. (n.d.). %5Curl%7Bhttps://climatedata.ca/resource/idf-curves-101/%7D

Kao, S.-C., & Ganguly, A. R. (2011). Intensity, duration, and frequency of precipitation extremes under 21st-century warming scenarios. *Journal of Geophysical Research: Atmospheres*, *116*. https://doi.org/10.1029/2010JD015529

Kharin, V. V., Zwiers, F. W., Zhang, X., & Wehner, M. (2013). Changes in temperature and precipitation extremes in the CMIP5 ensemble. *Climatic Change*. https://doi.org/10.1007/s10584-013-0705-8

Kidston, J., Dean, S. M., Renwick, J. A., & Vallis, G. K. (2010). A robust increase in the eddy length scale in the simulation of future climates. *Geophysical Research Letters*, *37*. https://doi.org/10.1029/2009GL041615

Kirsch, T. D., Wadhwani, C., Sauer, L., Doocy, S., & Catlett, C. (2012). Impact of the 2010 pakistan floods on rural and urban populations at six months. *PLOS Curr.* https://doi.org/10.1371/4fdfb212d2432

Li, Z., & O'Gorman, P. A. (2020). Response of vertical velocities in extratropical precipitation extremes to climate change. *Journal of Climate*, *33*. https://doi.org/10.1175/JCLI-D-19-0766.1

Lu, J., Leung, L. R., Yang, Q., Chen, G., Collins, W. D., Li, F., Hou, Z. J., & Feng, X. (2014). The robust dynamical contribution to precipitation extremes in idealized warming simulations across model resolutions. *Geophysical Research Letters*, *41*. https://doi.org/10.1002/2014GL059532

Milrad, S. M., Gyakum, J. R., & Atallah, E. H. (2015). A Meteorological Analysis of the 2013 Alberta Flood: Antecedent Large-Scale Flow Pattern and Synoptic–Dynamic Characteristics. *Monthly Weather Review*. https://doi.org/10.1175/MWR-D-14-00236.1

Mpanza, M. A. T., & Tandon, N. F. (2022). Further probing the mechanisms driving projected decreases of extreme precipitation intensity over the subtropical atlantic. *Climate Dynamics*, *59*. https://doi.org/10.1007/s00382-022-06268-3

Nie, J., & Sobel, A. H. (2016). Modeling the interaction between quasigeostrophic vertical motion and convection in a single column. *Journal of the Atmospheric Sciences*, *73*. https://doi.org/10.1175/JAS-D-15-0205.1

O'Gorman, P. A. (2015). Precipitation extremes under climate change. *Current Climate Change Reports*, *1*. https://doi.org/10.1007/s40641-015-0009-3

O'Gorman, P. A. (2012). Sensitivity of tropical precipitation extremes to climate change. *Nature Geoscience*. https://doi.org/10.1038/ngeo1568

O'Gorman, P. A., & Schneider, T. (2009a). Scaling of precipitation extremes over a wide range of climates simulated with an idealized gcm. *Journal of Climate*, *22*. https://doi.org/10.1175/2009JCLI2701.1

O'Gorman, P. A., & Schneider, T. (2009b). Scaling of precipitation extremes over a wide range of climates simulated with an idealized gcm. *JOURNAL OF CLIMATE*, *106*. https://doi.org/10.1073/pnas.0907610106

Park, I.-H., & Min, S.-K. (2017). Role of convective precipitation in the relationship between subdaily extreme precipitation and temperature. *Journal of Climate*, *30*. https://doi.org/10.1175/JCLI-D-17-0075.1

Pfahl, S., O'Gorman, P. A., & Fischer, E. M. (2017). Understanding the regional pattern of projected future changes in extreme precipitation. *Nature Climate Change*. https://doi.org/10.1038/nclimate3287

Roca, R., & Fiolleau, T. (2020). Extreme precipitation in the tropics is closely associated with long-lived convective systems. *Communications Earth & Environment*. https://doi.org/10.1038/s43247-020-00015-4

Tandon, N. F., Zhang, X., & Sobel, A. H. (2018). Understanding the dynamics of future changes in extreme precipitation intensity. *Geophysical Research Letters*, *45*. https://doi.org/10.1002/2017GL076361

Xie, P., Joyce, R., Wu, S., Yoo, S.-H., Yarosh, Y., Sun, F., Lin, R., & NOAA CDR Program. (2019). NOAA Climate Data Record (CDR) of CPC Morphing Technique (CMORPH) High Resolution Global Precipitation Estimates, Version 1. *NOAA National Centers for Environmental Information*. https://doi.org/10.25921/w9va-q159

Zhu, J., Otto-Bliesner, B. L., Brady, E. C., Gettelman, A., Bacmeister, J. T., Neale, R. B., Poulsen, C. J., Shaw, J. K., McGraw, Z. S., & Kay, J. E. (2022). Lgm paleoclimate constraints inform cloud parameterizations and equilibrium climate sensitivity in cesm2. *Journal of Advances in Modeling Earth Systems*, *14*. https://doi.org/10.1029/2021MS002776